Resolving Power of Wave Gauge Array Installed
in Lake Biwa

By Masataka YAMAGUCHI, Yoshito TSUCHIYA and Hiroshi KOYATA

(Manuscript received March 31, 1977)

Abstract

In this paper, the resolving power of the wave gauge array for the measurement of directional spectra used in Lake Biwa is investigated, based on numerical simulation.

The evaluation method with the best resolving power and the applicability region of the wave gauge array used are considered, evaluating approximate directional spectra of two-dimensional random waves with the known spectra generated by numerical simulation for the array through several computational methods of directional spectra and comparing between input spectra and output spectra. It is found that the least square method proposed by Borgman produces good results as does the function fitting method, so that for a frequency region containing the main energy of wind waves generated in Lake Biwa, better estimation of directional spectra is possible to be attained in applying these methods to the array.

1. Introduction

It is needless to say that the investigation of directional spectra of wind waves is indispensable to more precise understanding of various phenomena pertaining to coastal engineering. Because of the difficulty of measurement and analysis of directional spectra compared to those of frequency spectra, directional spectra which have a distinct relation with the field of winds have not been obtained except for a small number of examples such as the results by Cote et al.[1], by Longuet-Higgins et al.[2] and by Mitsuyasu et al.[3].

A wave observation[4] using a number of capacitance type wave gauges was conducted in Lake Biwa for one year from 1975 in cooperation with the Division of Coastal Engineering in the Department of Civil Engineering. In the observation, directional spectra of wind waves in limited fetch were measured by an array composed of 8 wave gauges.

In the investigation on characteristics of directional spectra, one of the most important problems is to make clear the resolving power of the array used.

Investigation on directional resolving power of arrays was first made by Barber,[5] using Eq. (3) mentioned below, which is the beam-forming pattern of array. After Barber, Panicker and Borgman,[6] Panicker[7] and Chakrabarti et al.[8],[9] investigated resolving power of various arrays using simple harmonic waves with one or more directions, while Fan[10] and Suzuki[11] employed irregular waves with known directional spectra simulated on a digital computer in their investigations.

In this paper, approximate directional spectra of irregular waves with the known

ones generated by numerical simulation are computed by many previously proposed computational methods, and from the comparison between the input spectra and the output spectra, some considerations are made to find out the computational method with the best resolving power of the present methods and the applicability of the array in evaluating directional spectra practically, based on the observed data.

2. Computational Methods of Directional Spectra

As fluctuation of the sea surface has a three dimensional property, directional spectra must be essentially defined by the triple Fourier transform of the correlogram on two horizontal space coordinates (x, y) and time t. However, because of the practical impossibility to measure directional spectra by this definition, the following three methods depending on the dispersion relation of the small amplitude wave theory, are often used for measurement of directional spectra.

(i) The method using spatial distribution of waves measured simultaneously; stereophotographic technique, optical analogue technique and radio backscattering technique

(ii) The method using time variation of surface displacement measured at a small number of points; wave gauge array technique

(iii) The method using vector quantities of waves measured at a point; buoy technique, current meter technique, wave force meter technique and wave gauge array technique.

The purpose of measurement by the wave gauge array installed in Lake Biwa is to combine method (ii) with method (iii).

A number of methods for evaluating directional spectra have been extended by many researchers since proposed by Barber. Under the presupposition of random phase mode of analysis and full circle analysis advanced by Panicker, these methods are classified as shown in Table 1. Summary of the methods used in this paper is as follows;

Table 1 Classification of computational methods of directional spectrum.
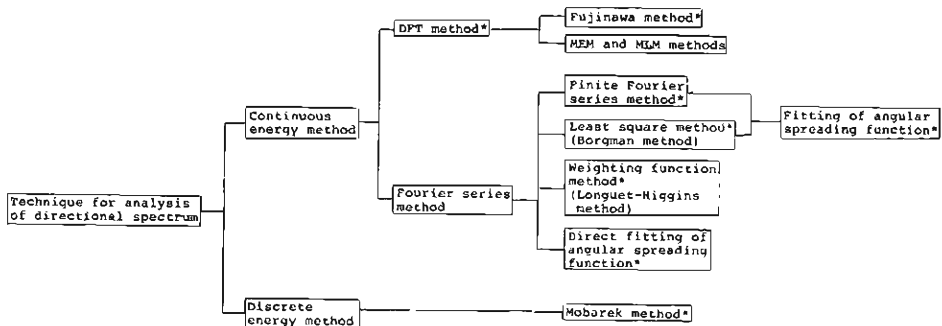
The method followed by the asterisk was used in this paper.

(a)   The Direct Fourier Transform method and the Fujinawa method

The expression for computing directional spectra $E(f, \theta)$ by the Direct Fourier Transform method (DFT method) is written as

$$E(f, \theta) = \sum_{ij} [c_{ij}(f) \cos\{kD_{ij} \cos(\theta - \beta_{ij})\}$$
$$+ q_{ij}(f) \sin\{kD_{ij} \cos(\theta - \beta_{ij})\}] \tag{1}$$

in which f is the frequency, θ the azimuth, $c_{ij}(f)$ the cospectrum, $q_{ij}(f)$ the quadrature spectrum, k the wave number, D_{ij} the distance between each wave gauge and β_{ij} the angle of wave gauge pair line with reference axis, respectively. The number of the term to be added in Eq. (1) is the one of the wave gauge pairs. Eq. (1) means that the measured directional spectrum $E(\theta)$ for a fixed frequency is the result of convolution of the true spectrum $E'(\theta')$ with a given factor $H(\theta, \theta')$ that is uniquely determined from the configuration of wave gauges, that is, Eq. (1) is expressed as

$$E(\theta) = \int_{-\pi}^{\pi} H(\theta, \theta') E'(\theta') d\theta' \tag{2}$$

with

$$H(\theta, \theta') = 1 + 2 \sum_{ij} \cos[kD_{ij}\{\cos(\theta - \beta_{ij}) - \cos(\theta' - \beta_{ij})\}] \tag{3}$$

Eq. (1) is the Fredholm integral equation of the first kind.

Fujinawa[12] proposed a new method for evaluation of directional spectra by solving Eq. (2) through the Fourier series expansion method. Expanding $E(\theta)$, $E'(\theta')$ and $H(\theta, \theta')$ in the Fourier series, Eq. (2) yields

$$\sum_{n=-\infty}^{\infty} a_{mn} z_{-n} = \frac{d_m}{2\pi} ; \quad -\infty < m < \infty \tag{4}$$

in which d_m, z_{-n} and a_{mn} are the Fourier coefficients of $E(\theta)$, $E'(\theta')$ and $H(\theta, \theta')$, respectively. The true directional spectrum can be obtained as the sum of infinite Fourier series by solving the linear simultaneous equation, Eq. (4). The Fourier coefficients are easily obtained making use of FFT algorithm.

(b)   The Fourier series method

Directional spectrum is conveniently expressed in the form

$$E(f, \theta) = E(f) D(\theta) \tag{5}$$

with

$$\int_{-\pi}^{\pi} D(\theta) d\theta = 1 \quad \text{and} \quad E(f) = \int_{-\pi}^{\pi} E(f, \theta) d\theta \tag{6}$$

in which $E(f)$ is the frequency (one-dimensional) spectrum and $D(\theta)$ the angular spreading function. If $D(\theta)$ is expanded in the Fourier series as

$$D(\theta) = \frac{1}{2\pi} + \sum_{n=1}^{\infty} (a_n \cos n\theta + b_n \sin n\theta) \tag{7}$$

the equations to determine the coefficients are given as

$$
\left.
\begin{aligned}
c'(f) &= J_0(kD) + 2\pi \sum_{n=1}^{\infty} (-1)^n J_{2n}(kD)(a_{2n}\cos 2n\beta + b_{2n}\sin 2n\beta) \\
q'(f) &= 2\pi \sum_{n=1}^{\infty} (-1)^{n+1} J_{2n-1}(kD)\{a_{2n-1}\cos(2n-1)\beta + b_{2n-1}\sin(2n-1)\beta\}
\end{aligned}
\right\}
$$
(8)

in which $J_n(kD)$ is the Bessel function of the first kind, $c'(f) = c(f)/E(f)$ and $q'(f) = q(f)/E(f)$. For brevity, the subscript ij of c', q', D and β is abbreviated in Eq. (8).

A finite Fourier series method is the computational method of directional spectra using directly the coefficients obtained from Eq. (8). Borgman[3] proposed a method to determine the coefficients in Eq. (8) by the least square method in order to avoid many instabilities with numerical computations. Since meaningless oscillation around zero level (side lobe) inevitably appears more or less in the directional spectra from both the methods mentioned above, Borgman also proposed two methods to avoid this side lobe as much as possible. The one is a weighted modification of the finite Fourier series used firstly by Longuet-Higgins. Applying a non-negative weighting function $R_N \cos^{2N}(\theta/2)$, angular spreading function is smoothed as

$$
D(\theta) = \frac{1}{2\pi} + \sum_{n=1}^{N} c_n(a_n\cos n\theta + b_n\sin n\theta)
$$
(9)

with

$$
R_N = \frac{\prod\limits_{i=1}^{N}(2i)}{2\pi \prod\limits_{i=1}^{N}(2i-1)} \quad \text{and} \quad c_n = \frac{2\pi R_N}{4^N} {}_{2N}C_{N-n}
$$
(10)

The smoothing is attained at the sacrifice of broadening the directional spectra and decreasing the value of spectral peak, even if more terms in the Fourier series are used for the representation of directional spectra.

The other is a method fitting a function such that the general shape of $D(\theta)$ except for the unknown fitting constants, is known in advance to the angular spreading function under the assumption that directional spectra is unimodal. Longuet-Higgins used a distribution function of $\cos^{2S}(\theta/2)$ and Borgman proposed a circular normal distribution in addition to the other two functions. Although tedious computation is required to estimate the unknown parameters, the method may be applicable to the bimodal directional spectra, if some corrections are made.

A circular normal distribution is expressed in terms of the modified Bessel function of order 0, $I_0(a)$ as

$$
D(\theta) = \frac{\exp\{a\cos(\theta-\theta_0)\}}{2\pi I_0(a)}
$$
(11)

in which θ_0 is the direction of the maximum in angular spreading function and a the concentration coefficient, which represents the degree of concentration of wave energy in a certain direction. A circular normal distribution can be expanded in the

form of

$$D(\theta) = \frac{1}{2\pi} + \sum_{n=1}^{\infty} \frac{I_n(a)}{\pi I_0(a)} (\cos n\theta_0 \cos n\theta + \sin n\theta_0 \sin n\theta) \tag{12}$$

in which $I_n(a)$ is the modified Bessel function of order n.   The number of the parameters to be evaluated is two in Eqs. (11) and (12) respectively.   From the comparison of Eq. (7) with Eq. (12), the following relations are immediately obtained.

$$a_n = \frac{I_n(a)}{\pi I_0(a)} \cos n\theta_0, \quad b_n = \frac{I_n(a)}{\pi I_0(a)} \sin n\theta_0 \tag{13}$$

Borgman describes a method to evaluate the parameters, making use of Eq. (13) for $n=1$.   The parameters can be also estimated by the least square method as

$$\frac{\partial Q}{\partial a} = 0, \quad -\frac{\partial Q}{\partial \theta_0} = 0 \tag{14}$$

with

$$Q = \sum_{n=1}^{N} \left\{ \left(a_n - \frac{I_n(a)}{\pi I_0(a)} \cos n\theta_0 \right)^2 + \left(b_n - \frac{I_n(a)}{\pi I_0(a)} \sin n\theta_0 \right)^2 \right\} \tag{15}$$

As the Fourier coefficient of lower order is more exact, the weighted least square method may be preferable.   The equation is given as

$$Q = \sum_{n=1}^{N} \left\{ \left(a_n - \frac{I_n(a)}{\pi I_0(a)} \cos n\theta_0 \right)^2 + \left(b_n - \frac{I_n(a)}{\pi I_0(a)} \sin n\theta_0 \right)^2 \right\} (N-n+1) \tag{16}$$

The relation between the cross spectra and the parameters mentioned above is obtained from Eqs. (8) and (13) as

$$\left. \begin{aligned} c'(f) &= J_0(kD) + \frac{2}{I_0(a)} \sum_{n=1}^{\infty} (-1)^n I_{2n}(a) J_{2n}(kD) \cos 2n(\beta - \theta_0) \\ q'(f) &= \frac{2}{I_0(a)} \sum_{n=1}^{\infty} (-1)^{n+1} I_{2n-1}(a) J_{2n-1}(kD) \sin (2n-1)(\beta - \theta_0) \end{aligned} \right\} \tag{17}$$

The parameters, a and θ_0 are evaluated from Eq. (17) by the least square method as well as Eq. (14).   This method is very useful in evaluating the parameters by an array of lesser wave gauges.   Numerical computation can be easily performed by a combination with the Newton iterative technique and a regula-falsi method.

The lower order Fourier coefficients can be directly obtained from power spectra and cross spectra between vector quantities of waves at a point such as surface displacement and wave slopes of two components, as the principle was firstly described by Longuet-Higgins.   Once the coefficients are obtained, the weighted modification method of the finite Fourier series and the function fitting method of the circular normal distribution can be applied, as mentioned above.   Horiguchi[14] proposed a method to measure directional spectra by a plus-shaped array of 5 wave gauges.   The computational method of directional spectra is almost the same as the one by Longuet-Higgins, if some corrections are added.

(c)   The discrete energy method

If the wave energy e_1, e_2, ... e_d is concentrated in a finite number of directions θ_1, θ_2, ... θ_d, the relation for any particular frequency between the discrete wave energy and the cross spectra obtained from a wave gauge array is given by Mobarek[15] as

$$c(f) + iq(f) = \sum_{j=1}^{d} e_j \exp \{ikD \cos (\theta_j - \beta)\} \tag{18}$$

in which $e_j (j=1 \sim d)$ is the wave energy of each direction and d the number of the assumed wave direction.   In practical computation, the least square method is used to avoid numerical instability, as done by Mobarek and Fan.

3. Numerical Simulation of Two-Dimensional Waves

(1) Wave gauge array used
      Various types of wave gauge arrays such as a line array, star-shaped array and so on have been investigated to measure directional spectra. As mentioned previously, the wave gauge array used in this paper has the properties of both combined wave gauge array technique with buoy technique.
      Fig. 1 shows the configuration of the wave gauge array installed in Lake Biwa and its setting depth in water.   The array of plus-shaped (N-4~N-8) set on the observation tower has the property of detecting directional spectra by measuring surface displacement at a point and its slope and curvature of the components for longer period waves (the Horiguchi method) and by measuring surface displacement at five points for shorter period waves.   Four wave gauges composed of 1 wave gauge at the center of the tower (N-8) and 3 wave gauges around the tower (N-9 ~N-11) constitute a well-known star-shaped array, and 8 wave gauges collectively consititute an array with better resolving power than a star-shaped array. Maximum distance between wave gauges is 10 m − 11 m, and then the array gives the best resolving power for the predominant waves of which periods are about 3 sec, in
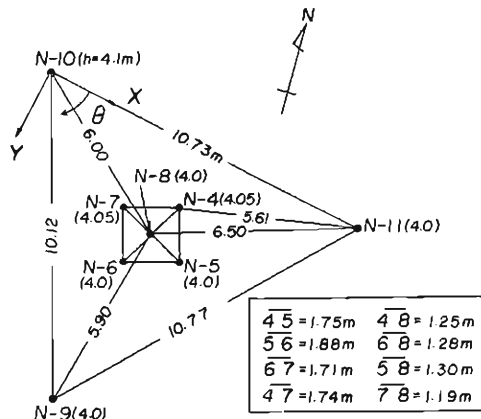

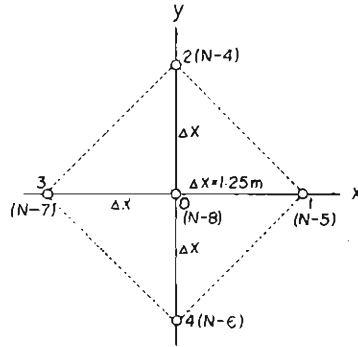
Fig. 1 Configuration of wave gauge array used.

Fig. 2 Coordinate system used in the Horiguchi method.

Lake Biwa.

Fig. 2 shows the coordinate system in evaluating directional spectra by the Horiguchi method which is in principle the same method as the buoy technique.

(2) Numerical simulation of random waves

A systematic study on random wave simulation was done by Borgman[16] and successive studies have been continued by Fan, Suzuki, Goda[17] and Iwagaki et al.[18] There are, however, few examples of numerical simulation of directional spectra, except for the results by Fan and by Suzuki.

According to Pierson, the surface displacement of random seas is discretely expressed as

$$\eta(x, y, t) = \lim_{M \to \infty} \lim_{N \to \infty} \sum_{m=1}^{M} \sum_{n=1}^{N} \sqrt{2E(\hat{f}_m, \hat{\theta}_n) \overline{\Delta f_m \Delta \theta_n}} \cos (\hat{k}_m x \cos \hat{\theta}_n + \hat{k}_m y \sin \hat{\theta}_n - 2\pi \hat{f}_m t + \phi_{mn}) \tag{19}$$

in which ϕ_{nn} is the independent random variable distributed uniformly over interval $(0, 2\pi)$. The variables, $\hat{f}_m$, $\hat{\theta}_n$, Δf_m and $\Delta \theta_n$ are defined respectively as

$$\hat{f}_m = \frac{f_{m-1} + f_m}{2}, \quad \hat{\theta}_n = \frac{\theta_{n-1} + \theta_n}{2}$$
$$\Delta f_m = f_m - f_{m-1}, \quad \Delta \theta_n = \theta_n - \theta_{n-1} \tag{20}$$

and $\hat{k}_m$ is also defined by the dispersion relation of the small amplitude wave theory as

$$(2\pi \hat{f}_m)^2 = g \hat{k}_m \tanh \hat{k}_m h \tag{21}$$

In the simulation, it is important to select a model frequency spectrum and angular spreading function as the target spectrum. As wind waves in Lake Biwa have fetch-limited spectra, the JONSWAP spectrum proposed by Hasselmann et al.[19], based on wave observation in the North Sea, was adopted as the target frequency spectrum. It is expressed as

$$E(f) = \alpha g^2 (2\pi)^{-4} f^{-5} \exp\left[-\frac{5}{4}\left(\frac{f}{f_{max}}\right)^{-4}\right] \gamma^{\exp\left\{-\frac{(f-f_{max})^2}{2\sigma^2 f^2_{max}}\right\}} \tag{22}$$

with

$$\left.\begin{array}{l} \alpha = 0.076\tilde{x}^{-0.22}, \quad \dfrac{f_{max}U_{10}}{g} = 3.5\tilde{x}^{-0.33} \\[2mm] \tilde{x} = \dfrac{gF}{U_{10}^2}, \quad \gamma = 3.3, \quad \sigma = \begin{cases} 0.07 \; ; f \leq f_{max} \\ 0.09 \; ; f > f_{max} \end{cases} \end{array}\right\} \tag{23}$$

in which F is the fetch, f_{max} the peak frequency in one-dimensional spectrum, U_{10} the wind speed at the height of 10 m over the sea surface and $\tilde{x}$ the nondimensional fetch, respectively.

On the other hand, as the characteristics of angular spreading function of wind waves are not necessarily made clear in the present stage, the $\cos^n\theta$ type function ($n = 2$, 4, 8 and 16) and the circular normal distribution ($a = 6$ and 12) irrelevant to the frequency were used. The general form of the former is expressed as

$$D(\theta) = \begin{cases} \dfrac{\Gamma\left(\dfrac{n+2}{2}\right)}{\sqrt{\pi}\,\Gamma\left(\dfrac{n+1}{2}\right)} \cos^n(\theta-\theta_0) \; ; |\theta-\theta_0| \leq \dfrac{\pi}{2} \\[4mm] 0 \qquad\qquad\qquad\qquad ; |\theta-\theta_0| > \dfrac{\pi}{2} \end{cases} \tag{24}$$

in which Γ is the gamma function.

The two methods for simulating ocean wave processes are offered. These are (i) wave superposition and (ii) linear digital filter. Each method has advantages and disadvantages. The method by wave superposition was adopted, because the computation is very simple, although time-consuming.

In simulating by wave superposition, the selection of the frequency is very important, since the periodicity inevitably appears, in which case the frequency is divided into equal parts. Borgman proposed two methods to avoid this periodicity. The one is to select a set of f_m values with a random number table, and the other is to divide the frequency, based on the cummulative spectrum. In this study, the former method was used according to Goda's study, and the azimuth was divided into equal parts. The number of divisions for frequency and azimuth are 60 and 72, respectively. Table 2 shows the conditions of simulation.

In order to investigate the applicability of the wave superposition method, one-dimensional waves were simulated, using the JONSWAP spectrum and the Mitsuyasu II type spectrum. The comparison between the target spectrum and the realized one is shown in Fig. 3, in which case the number of data is 8192 and the degree of freedom is 256. In both the figures, good correspondence was attained except for the appearance of small oscillation at the higher frequency parts.

Fig. 4 is the frequency spectrum of two-dimensional waves simulated under the conditions given in Table 2. In comparison with the results of one-dimensional

Table 2   Conditions used in simulation.

frequency spectrum	JONSWAP spectrum	angular spreading function	$\cos^n\theta$ type and circular normal distribution
wind speed	10 m/sec	fetch	25.8 km
water depth	4 m	method of simulation	composite superposition
method of division f	division by random number	number of division f	60
method of division θ	equal division	number of division θ	72
range of f	$0.5f_{max}$ – $3.0f_{max}$	range of θ	$-90°$ – $90°$ and $-180°$ – $180°$
direction of peak energy	66°	sampling time	$1/15f_{max}$
number of gauges	8	computational method of spectrum	FFT method
number of data	3072 (1024x3)	degrees of freedom	90 (30x3)
filter	rectangular filter		
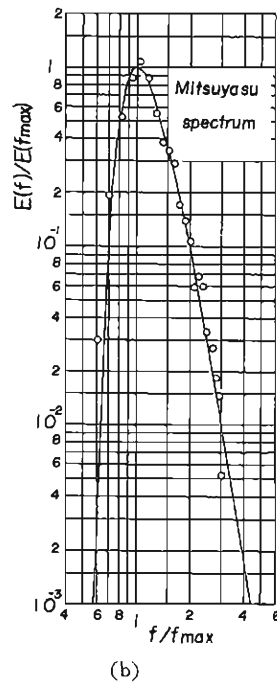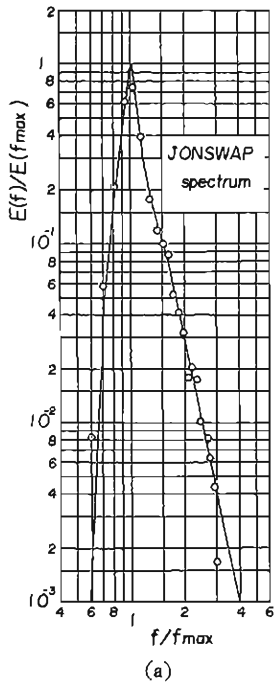
Fig. 3   Comparison between target spectrum and the realized one for one-dimensional waves.

waves shown in Fig. 3, although the correspondence becomes slightly poorer, it may be considered that the target spectrum is realized by this simulation.

Fig. 5 is the time variation of simulated waves.   The transformation of wave profile is appreciable, because the frequency dispersion of each component wave is predominant.
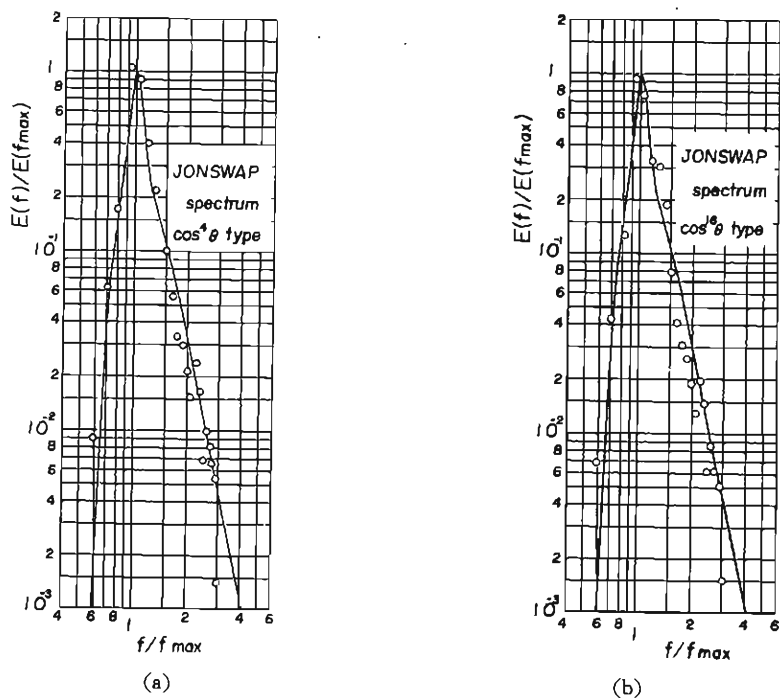
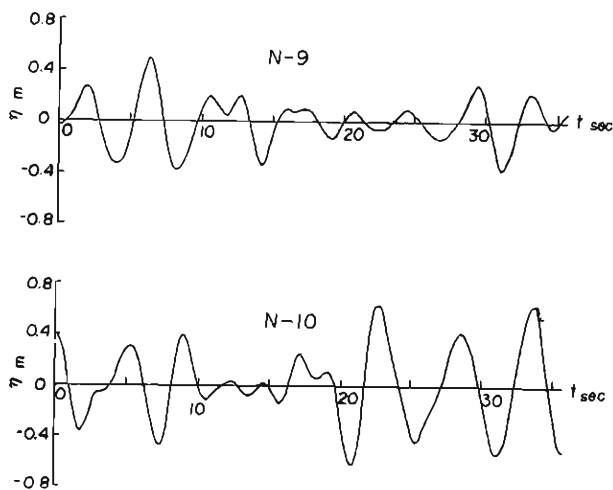Fig. 4   Comparison between target spectrum and the realized one for two-dimensional waves.

Fig. 5   Time variation of simulated waves.

4. Consideration on Resolving Power of the Array Used

4.1 Considerations on the simulation by the authors

(1) Applicability of the DFT method and the Fujinawa method

The resolving power of the array is investigated from the comparison between the given angular spreading function and the realized one estimated by the various methods, using at most 8 power spectra and 28 cross spectra obtained from the two-dimensional random wave simulation.

Fig. 6 is the angular spreading function evaluated by the DFT method for $\cos^4\theta$ type one, in which the solid line, broken line and one-dotted chain line designate the results computed from 4 wave gauges (star-shaped array), from 8 wave gauges and the given spreading function, respectively. In the figures, the 4 points method gives considerably good resolving power for $f=0.278$ cps, but for $f=0.309$ cps, remarkable smoothing and appearance of meaningless oscillation result in poor correspondence with the given spreading function. On the other hand, the 8 points method has poorer resolving power than the 4 points method, because a number of cross spectra not being independent of each other for the specified frequency, are summed up.

Fig. 7 is the result of the 5 points method (plus-shaped array) in the higher frequency region, which shows that the shape of the estimated function agrees rela-

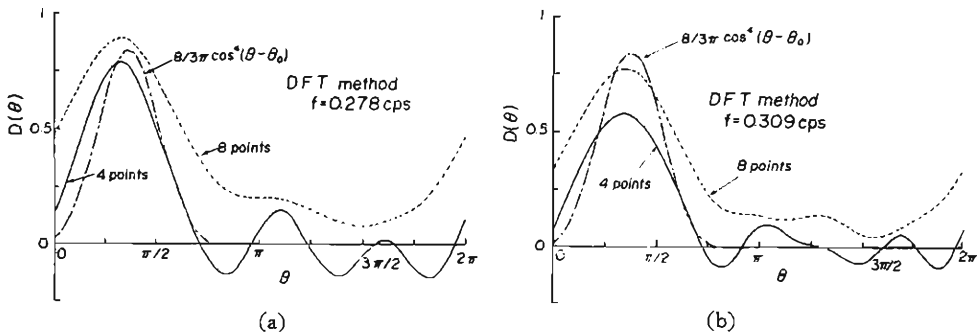
(a)   (b)

Fig. 6 Comparison between a given angular spreading function and one estimated by the DFT method (1).
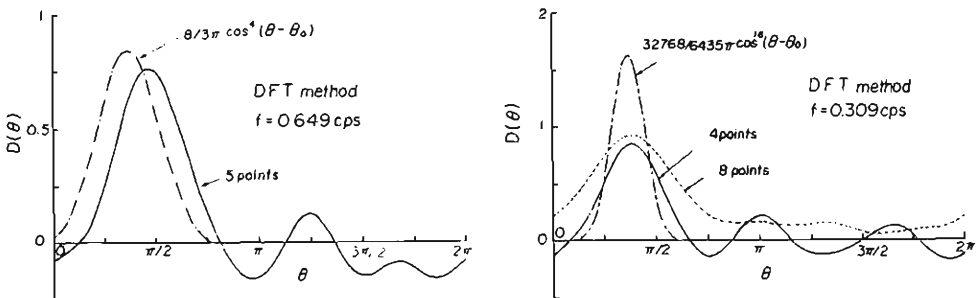

Fig. 7 Comparison between a given angular spreading function and one estimated by the DFT method (2).

Fig. 8 Comparison between a given angular spreading function and one estimated by the DFT method (3).

tively well with the given one, but a shift of direction of peak energy occurs.   As shown in Fig. 8, in the case of cos $^{16}\theta$ type function, in which the concentration of wave energy to a particular direction is high, considerable smoothing for the given spreading function is brought out even in a frequency region with good resolving power for cos $^4\theta$ type function.   As a result, it may be concluded that the effectiveness of the DFT method is questionable in evaluating directional spectra by two-dimensional array.

Fujinawa proposed a new method for the evaluation of directional spectra, and he asserted that the method has almost perfect resolving power for a certain range through a numerical computation of Eq. (4).   His simulation method is to compute the unknown Fourier coefficients of the true spectrum in Eq. (4), using Eq. (3) and the apparent spectrum obtained from Eq. (2) through numerical integration for the given array and directional spectrum. Fig. 9 shows some examples of the comparison between the results of his simulation method and the one by our simulation method for the present array in the case of cos $^4\theta$ type spreading function.   In this case, the number of wave gauges used is 8 and the number of terms truncated in the Fourier series is 4.   Hereafter, the notation such as F-8-4 and B-8-4 is used for brevity.   The first notation designates the first alphabet of the name of each researcher.   It follows that in using his simulation method, the Fujinawa method almost perfectly recovers the given spreading function for all the range of frequencies treated in this case, as indicated by Fujinawa, while at a certain frequency, considerable deviation from the given function appears in the results obtained through the Fujinawa method from the simulation of two-dimensional waves by the authors. Accordingly, it is doubtful whether his investigation on resolving power of wave gauge array is valid.

It is most important to determine the number of terms in the Fourier series to be used, in applying the Fujinawa method as well as the Borgman method mentioned below in the evaluation of directional spectra.   The sharper the shape of the angular spreading function becomes, the more terms in the Fourier series are needed to express the function exactly.   The evaluated angular spreading function is distorted, and meaningless oscillation becomes larger, if too many terms in the Fourier series

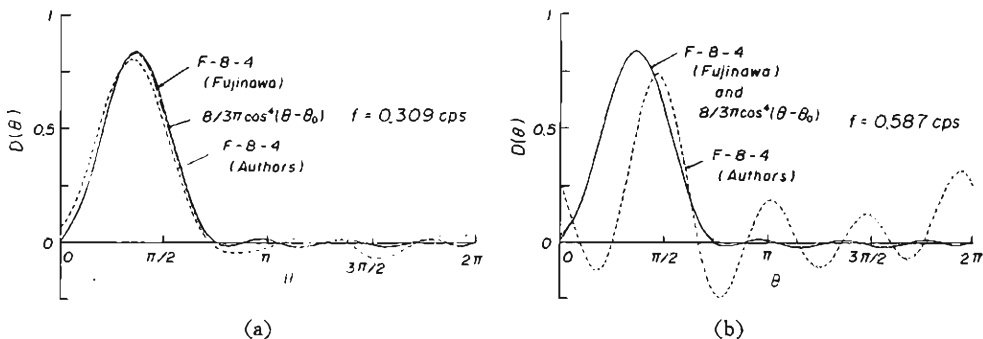(a)   (b)

Fig. 9 Comparison between a given angular spreading function and one estimated
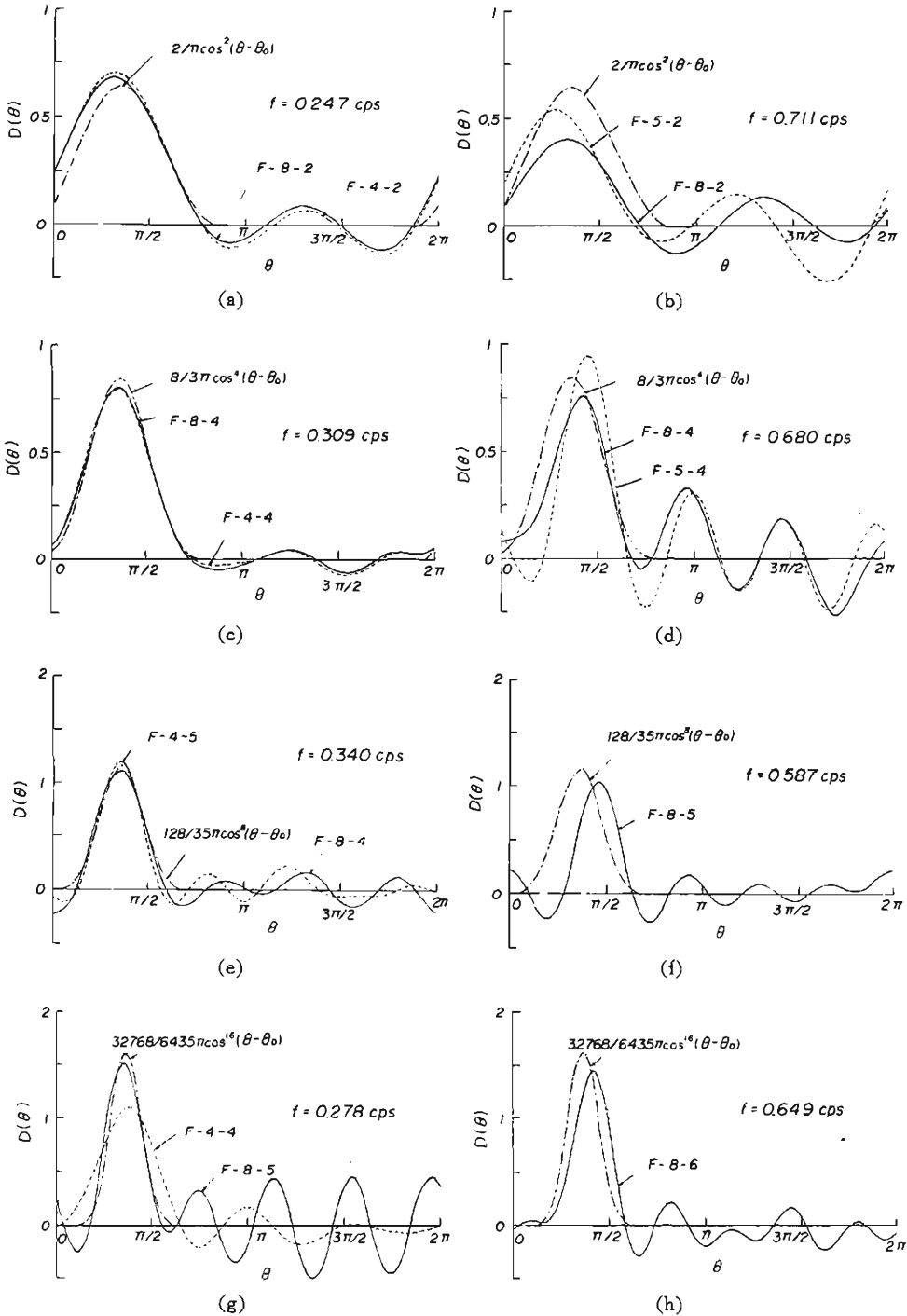   by the Fujinawa method (1).

Fig. 10 Comparison between a given angular spreading function and one estimated by the Fujinawa method (2).

are employed.   In the following, only the best result on resolving power for each wave gauge array is considered.

Fig. 10 shows some examples of the comparison between the results by the Fujinawa method and the given function for $\cos^2\theta$, $\cos^4\theta$, $\cos^8\theta$ and $\cos^{16}\theta$ type functions. It is found that the Fujinawa method gives good approximation to the given function for the lower frequency region, if the number of terms in the Fourier series is selected properly, and that the position of maximum in angular spreading function deviates appreciably from the given value.

(2)   Applicability of the Fourier series method

Fig. 11 shows the results obtained from star-shaped array by the finite Fourier series method (FFS method) and the weighting function method, in which $\cos^4\theta$ type function is used for the angular spreading function. The result for $f=0.309$ cps is the best one of all the results evaluated in this case.   In general, the FFS method is not suitable for practical use, because the method gives rise to numerical instability, as shown in the figure.   On the other hand, the weighting function method yields appreciable smoothing for the given function, and meaningless oscillation does not appear as expected.

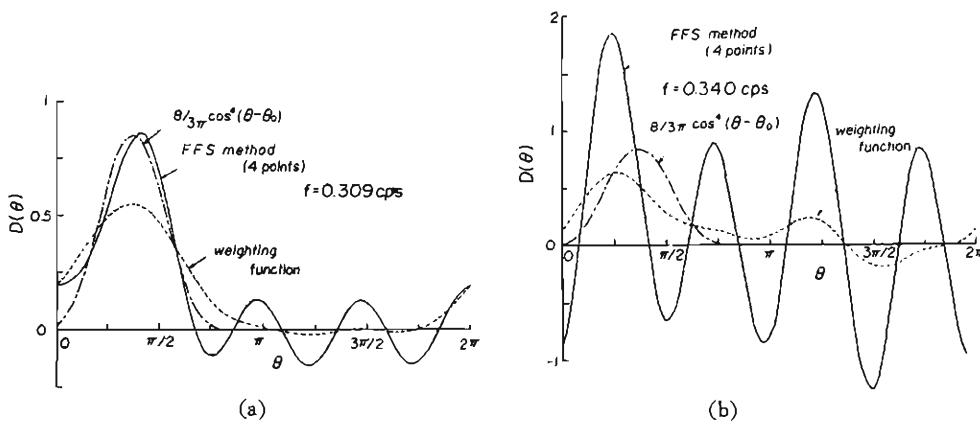(a)   (b)

Fig. 11   Comparison between a given angular spreading function and one estimated by the FFS method.

Fig. 12 shows some examples of the angular spreading function estimated by the Horiguchi method, using the plus-shaped array. In the figures, the solid line shows the result corresponding to the one by the FFS method without a weighting function and the dotted line is the result with a weighting function. Although the distance between each wave gauge is slightly different from each other and the diagonals do not cross at right angles, the distance Δx is assumed to be 1.25 m, neglecting these effects on the computed result. The result with a weighting function in Fig. 11 is to be truncated to the sixth term, while the result in Fig. 12 is to be truncated to the third term.   Accordingly, the shape of spreading function becomes sharper in the former case than in the latter case. Anyway, both the methods give poor correspondence with the given function.
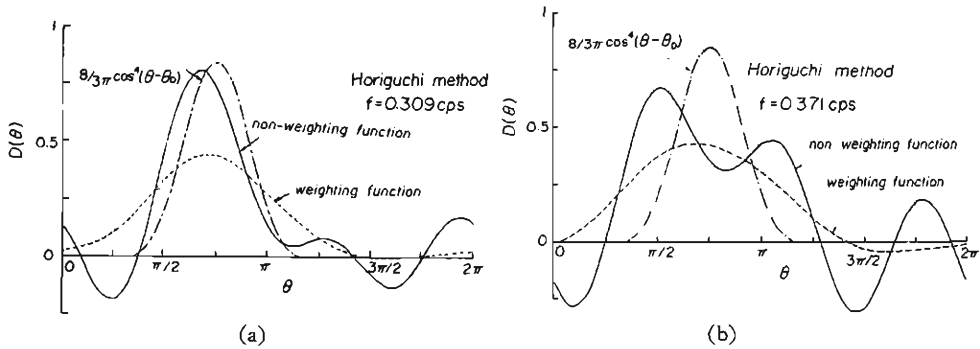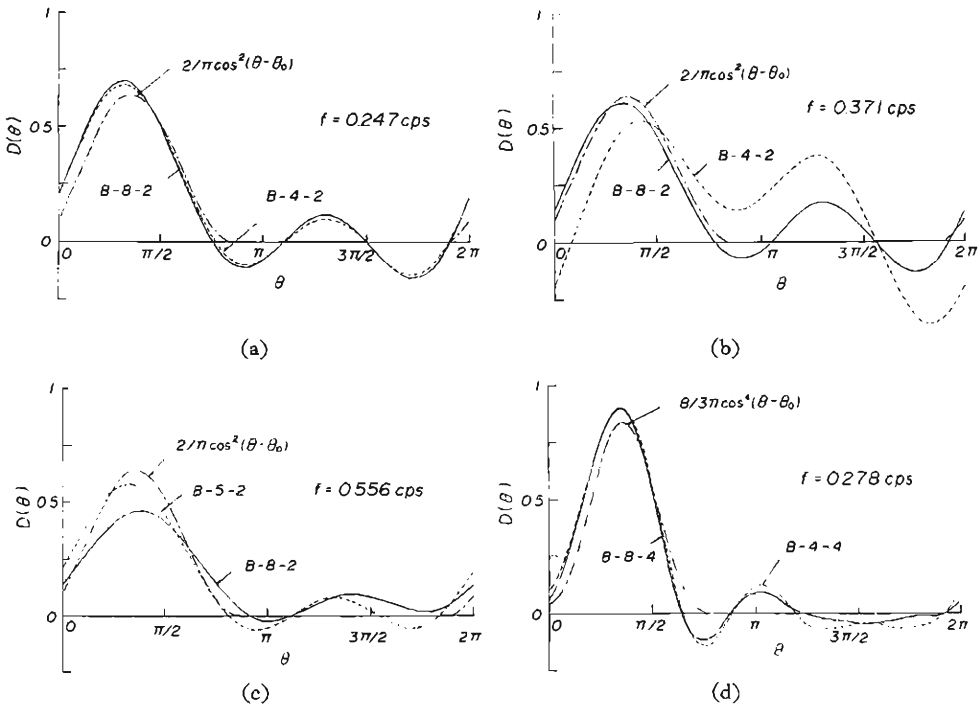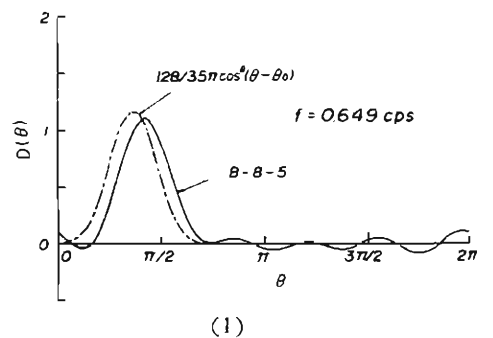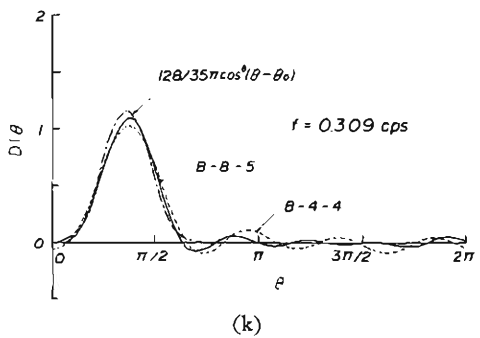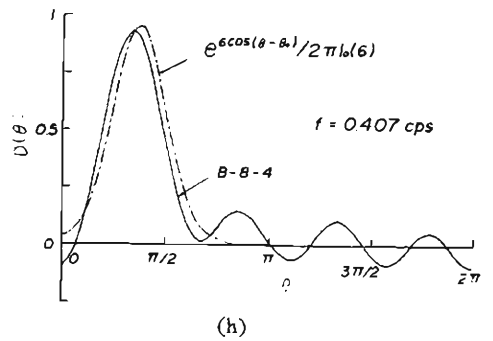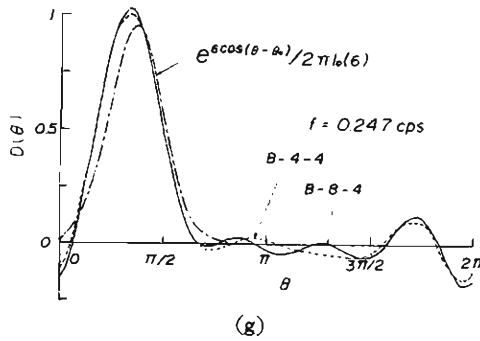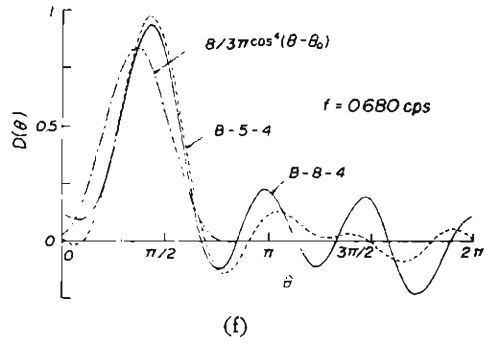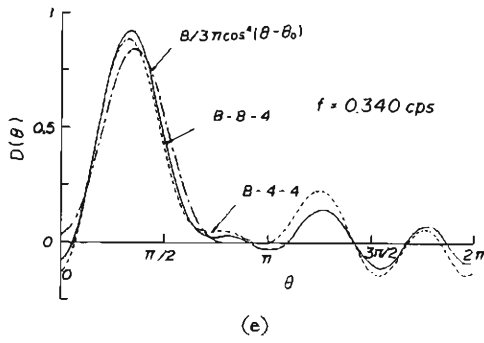
Fig. 12 Comparison between a given angular spreading function and one estimated by the Horiguchi method.

In Fig. 13, the applicability of the least square method proposed by Borgman is investigated in detail, because the method gives the best correspondence with the given function of all the methods treated in this paper. In the figures, the 4 points method has good resolving power as well as does the 8 points method in the smaller concentration coefficient, but with increase of the value, it gives a considerably smoothed curve. The frequency region which the 4 points method is applicable to the evaluation of directional spectra is narrower than the one by the 8 points method. On the other hand, the 5 points method produces better results than or almost equal to the result of the 8 points method in the smaller coefficient, while the method produces poor results in the larger coefficient.
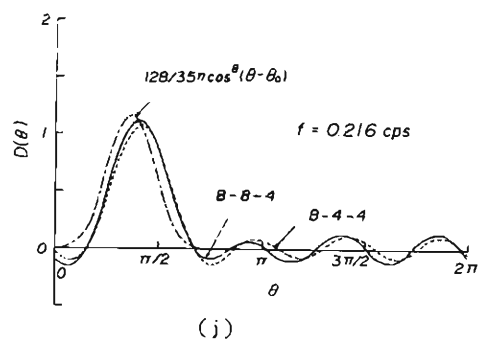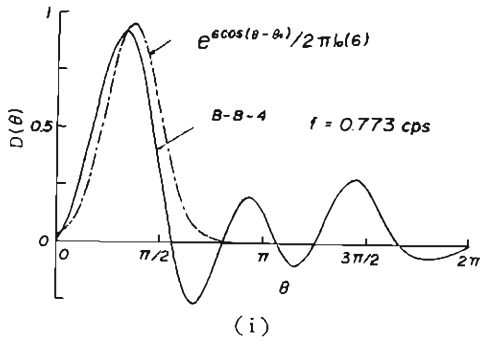
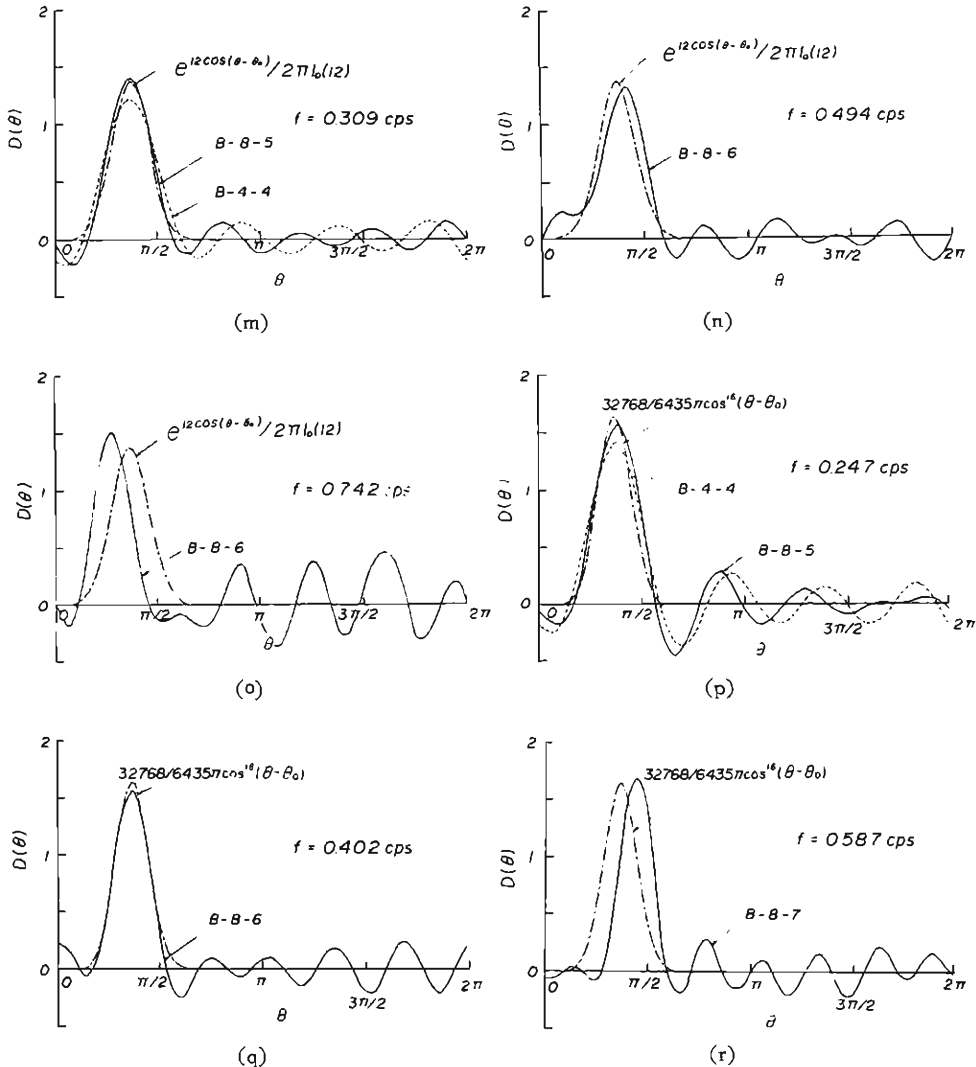(e)

(f)

(g)

(h)

(i)

(j)

(k)

(l)

Fig. 13 Comparison between a given angular spreading function and one estimated
by the Borgman method.

After all, it follows that the 8 points method has the best resolving power for
the wide range of frequency specified.   Even by the 8 points method, the direction
of the maximum in the angular spreading function tends to deviate from the given
direction in the higher frequency region.

Summarizing the result in Fig. 13, the number of wave gauges to be used and
the number of terms in the Fourier series to be truncated, in which case the best
resolving power is realized for each condition, are shown in Fig. 14.   In the figure,
the solid line means a frequency region giving good resolving power and the dotted
line a region giving poorer power compared to the former case.   It may be found
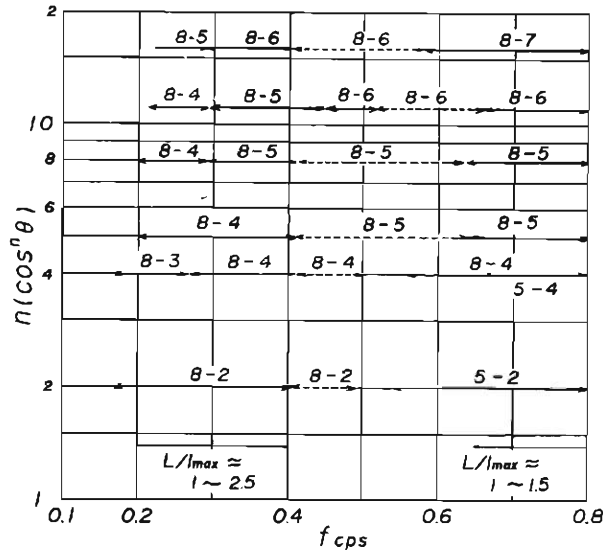
Fig. 14 Optimum number of terms in the Fourier series to be used
applying the Borgman method.

that the sharper the shape of spreading function becomes and the higher the
frequency becomes in the sharper function, the more the number of terms in the
Fourier series to be summed up becomes necessary in order to express the function
as exactly as possible.   The 8 points method gives better resolving power in the
frequency region of 0. 2 cps −0. 4 cps and 0. 65 cps −0. 8 cps, that is, the range of
L/l_{max} approximately changes from 1 to 2. 5 and from 1 to 1. 5 respectively, in which
L is the wave length and l_{max} the maximum distance between gauges.

Fig. 15 shows the resolving power of an array with 8 wave gauges, in which
case the angular spreading function with two peak mode,

$$D(\theta) = \begin{cases} 0 & ; -\pi < \theta < -\dfrac{\pi}{2} \\[2mm] \dfrac{64}{59\pi} \cos^4\theta & ; -\dfrac{\pi}{2} \leqq \theta \leqq 0 \\[2mm] \dfrac{64}{59\pi} \cos^4\theta + \dfrac{128}{59\pi} \cos^8\left(\theta - \dfrac{\pi}{2}\right) & ; 0 < \theta < \dfrac{\pi}{2} \\[2mm] \dfrac{128}{59\pi} \cos^8\left(\theta - \dfrac{\pi}{2}\right) & : \dfrac{\pi}{2} \leqq \theta \leqq \pi \end{cases} \tag{25}$$

is given as the input function. Even if the Borgman method as well as the Fujinawa
method are used in the evaluation, the methods produce poorer resolving power
compared to the case of angular spreading function with a single peak mode,
although it is possible to distinguish separately each maximum direction.

In applying a circular normal distribution to the fitting of the spreading function,
there are four methods expressed by Eqs. (13), (15), (16) and (17) as mentioned
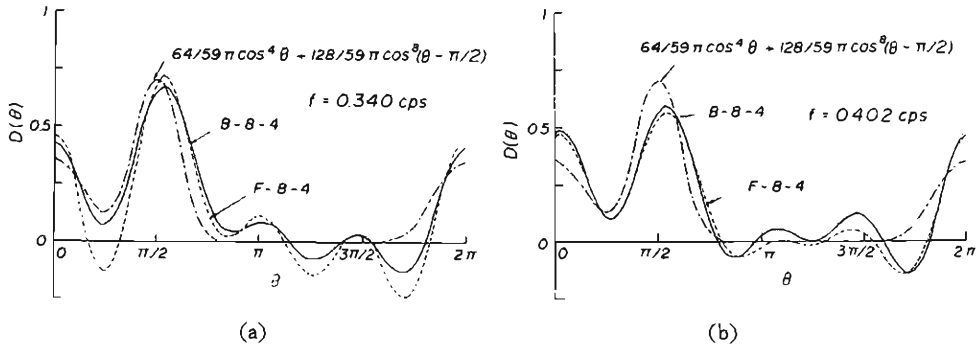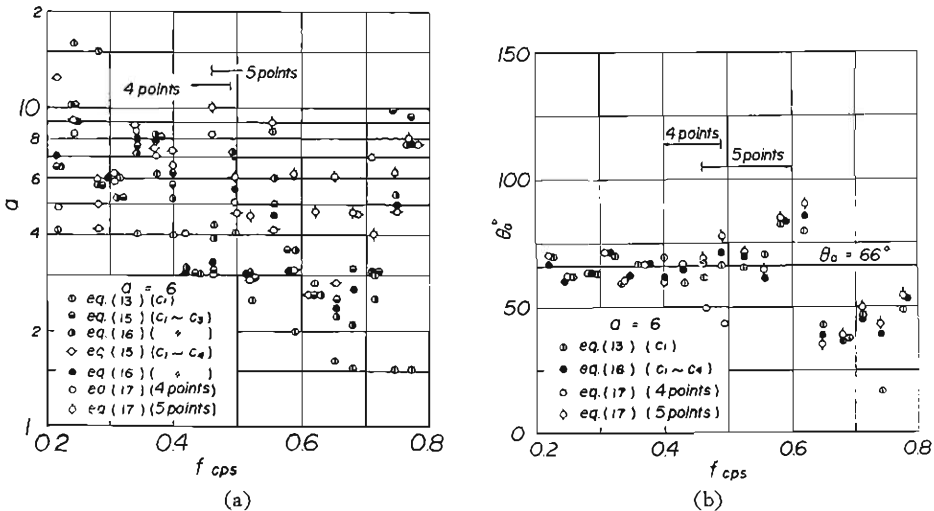
Fig. 15 Comparison between a given angular spreading function with two peak mode and one estimated by the Borgman method.

already. Fig. 16 shows the concentration coefficient and the peak direction in the spreading function estimated from the four methods for circular normal distributions of $a=6$ and $a=12$. Each method approximately produces the correct direction in the frequency region of 0.2 cps−0.55 cps, but in the higher frequency, the deviation from the given direction becomes larger as well as the one by the least square method by Borgman. On the other hand, the coefficient obtained from the first term in the Fourier series tends to be underestimated, and so the applicability becomes poorer with increase of the frequency. Although there appears some scatter in the coefficients estimated from Eqs. (15), (16) and (17) through the least square technique and the coefficient tends to be overestimated in case of larger coefficient, each of these methods gives valid results in a mean sense.

(3) Applicability of the discrete energy method

Fig. 17 shows the shape of the normalized angular spreading function obtained from the simulated data using the moving best fit method proposed by Mobarek in
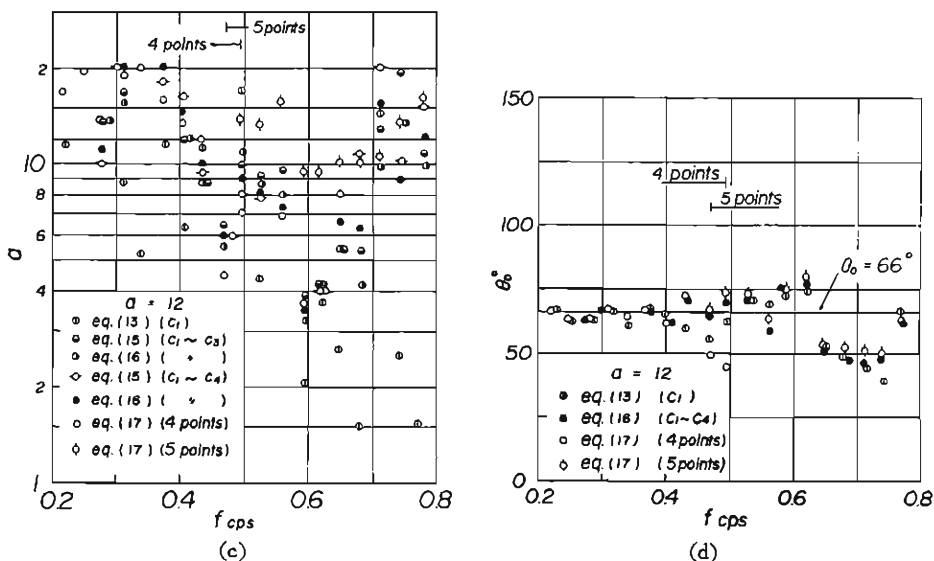
Fig. 16   Concentration coefficient and peak direction in angular spreading function estimated by the function fitting method.

Fig. 17   Comparison between a given angular spreading function and one estimated by the Mobarek method.

the case of star-shaped and plus-shaped arrays.

The selection of the number of wave directions is most important in applying the method.   A number of trials were performed and the best possible discrete energy was found using five points spaced 30 degrees as proposed by Chakrabarti et al.   In the case, the moving best fit method was applied by shifting the assumed wave directions at intervals of 5 degrees.   There are some cases where the discrete energy method makes the shape of the given function approximate fairly well, as shown in the figure.   However, it is inconvenient to apply the method for practical purposes, because the wave energy is expressed discretely in a finite number of directions.

4.2 Considerations based on the simulation by Fan

Fan simulated sea surface elevations in a digital computer for star-shaped array, using a linear digital filter method. The energy spectrum and the spreading function used are the Bretschneider-Pierson-Moskowitz type and the circular normal distribution, respectively. The conditions are $a=6$, $\theta_0=90°$, $l_{max}=11.3$ cm, $\Delta t=0.1$ sec and $N=2048$. The simulated data were cited by Borgman.

Fig. 18 shows the results obtained from the DFT method, the Fujinawa method and the Borgman method. The Borgman method produces good resolving power as does the Fujinawa method, because the ratio L/l_{max} is between 1 and 2.5, as can be expected from the above considerations, while the DFT method considerably smooths out the given function. Moreover, the deviation of maximum in the spreading function from the given direction is less in the Fan result than in the result by the authors.
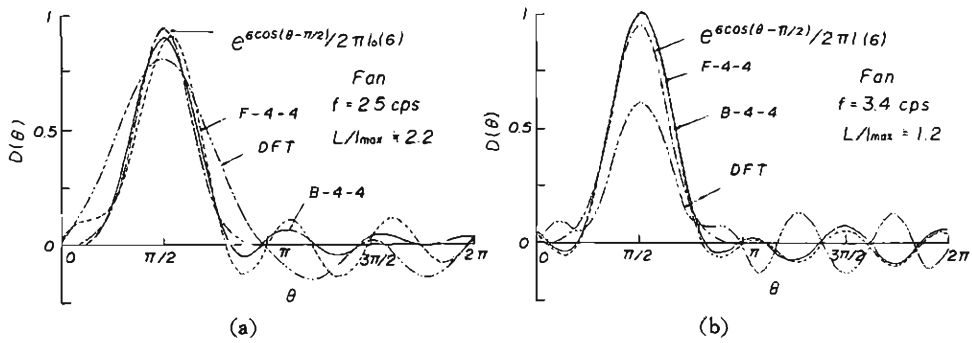
Fig 18 Comparison between a given angular spreading function and one by the DFT method, by the Borgman method and by the Fujinawa method, based on Fan's data.

Fig. 19 Concentration coefficient and peak direction in angular spreading function estimated by the function fitting method, based on Fan's data.
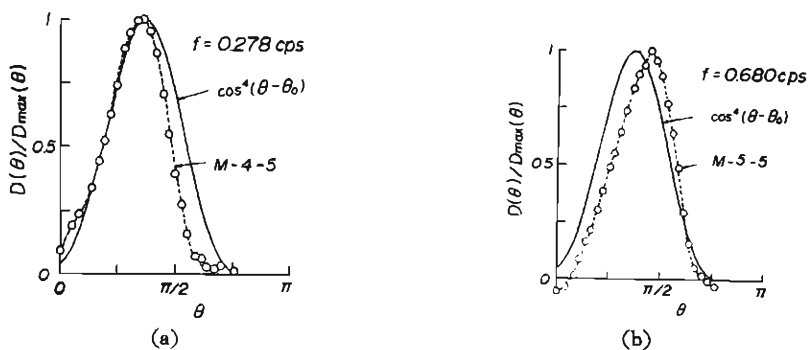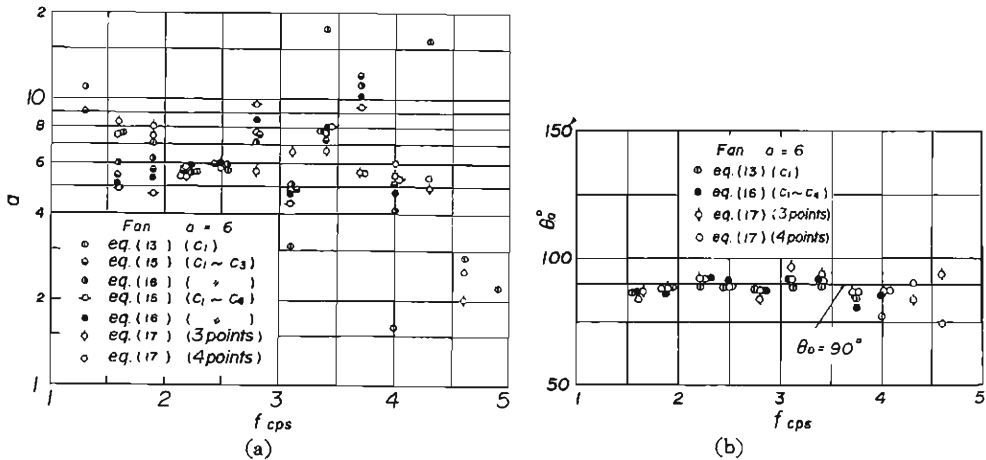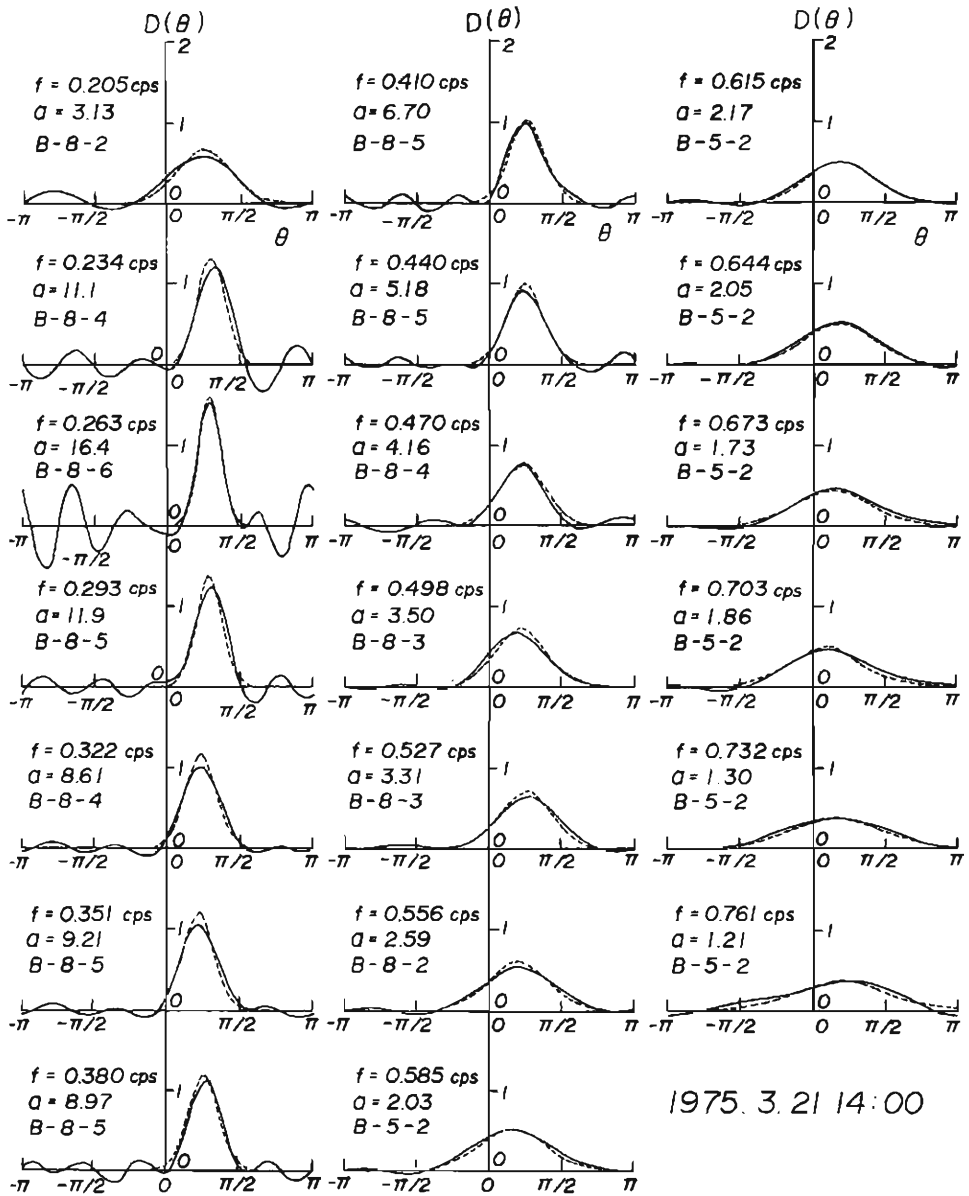
Fig. 20 Angular spreading function of wind waves in Lake Biwa estimated by the Borgman method and by the function fitting method.

The concentration coefficient and the peak direction obtained from the fitting methods of circular normal distribution are shown in Fig. 19.   In both the figures, the deviation in Fan's result from the given value is less appreciable than in the authors' result.   The applicability of the direct fitting method expressed by Eq. (17) is excellent compared to the other methods, especially the 3 points method using the regular triangular array is applicable for a wide frequency region.   Accordingly, the direct fitting method is very effective in the evaluation of directional spectra using the lesser wave gauges.

4.3 An example of directional spectra observed in Lake Biwa

Since March, 1975, wave observations using a number of capacitance-type wave gauges have been carried out in Lake Biwa in order to clarify fetch-limited directional spectra and wave tranformation in shoaling water.   A number of directional spectra were already evaluated from the observed data using the Borgman method and the fitting method of circular normal distribution. An example is shown in Fig. 20, in which the solid line and the dotted line designate the results obtained by the Borgman method and the direct fitting method under the conditions written in the respective figures. It is found that only if the number of terms in the Fourier series is properly selected according to the concentration coefficient obtained, the Borgman method produces better spreading function suppressing the meaningless oscillation as much as possible and that the result by the Borgman method has good correspondence with the one by the fitting method.

Fig. 21 is the concentration coefficient and the peak direction in the spreading function obtained from the function fitting method.   The concentration coefficients
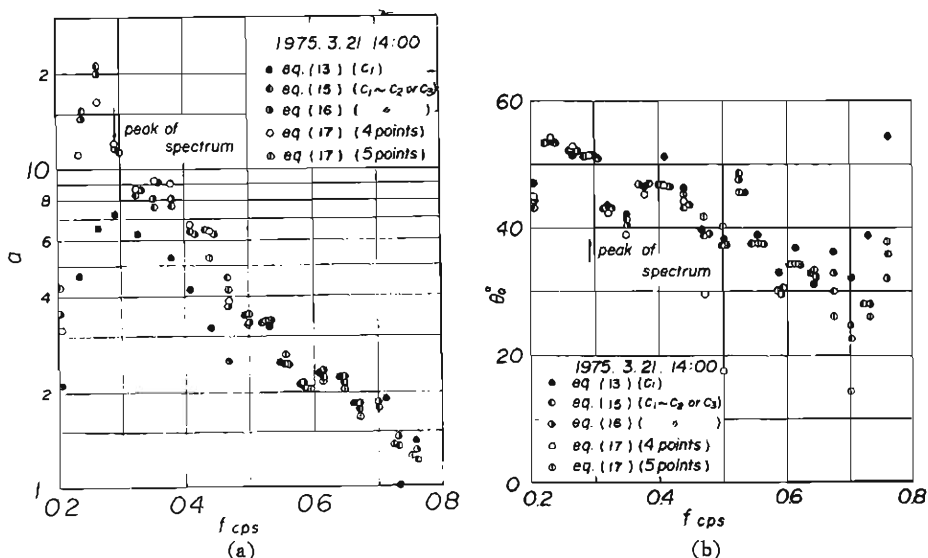

Fig. 21   Concentration coefficient and peak direction in angular spreading function in Lake Biwa estimated by the function fitting method.

obtained from the fitting methods are almost the same value as each other, except for the fitting method using only the first term in the Fourier series and it may be judged from the tendency of the evaluated coefficient that a valid result is obtained outside of the applicability region mentioned above.   The peak direction results in scattering to some extent in the higher frequency region, as may be expected from the above consideration.

The concentration coefficient becomes maximum near the peak frequency of frequency spectrum, and in the higher and the lower frequency, the coefficient gradually decreases.   The characteristics of directional spectra in a limited-fetch will be discussed in detail in a following paper.

5. Conclusions

In order to investigate the resolving power of the wave gauge array for measurement of directional spectra installed in Lake Biwa, two-dimensional random waves with known directional spectra were simulated on a digital computer using the method of composite superposition. The approximate directional spectra were evaluated by several methods, and the applicability of their methods was considered from the comparison between the given spectrum and the evaluated one.   It was found that if the number of terms in the Fourier series is properly selected according to the value of concenration coefficient in angular spreading function, the least square method by Borgman produces the most valid evaluation of the given function and a graph designating the optimum number of terms in the Fourier series to be used was proposed.   It was also found that in case of unimodal spreading function, the function fitting method in which the parameters are evaluated through the least square method is applicable to a wide frequency region.   In addition, an example of directional spectra estimated exactly as possible from the data observed in Lake Biwa was presented.

Acknowledgements

References

1)   Cote, L. J. et al.: The Directional Spectrum of a Wind Generated Sea as Determined from Data Obtained by the Stereo Wave Observation Project, Meteorological Paper, Vol. 2, No. 6, New York Univ., 1960, pp. 1-88.

2)   Longuet-Higgins, M. S., Cartwright, D. E. and N. D. Smith: Observations of the Directional Spectrum of Sea Waves Using the Motion of a Floating Buoy, Proc. Ocean Wave Spectra,

Prentice Hall, 1961, pp. 111-136.

3) Mitsuyasu, H. et al.: Observations of the Directional Spectrum of Ocean Waves Using a Cloverleaf Buoy, Jour. Phys. Oceanogr., Vol. 5, No. 4, 1975, pp. 750-760.

4) Iwagaki, Y. et al.: Wave Observations in Lake Biwa, Annuals, DPRI, Kyoto Univ., Vol. 19 B-2, 1976, pp. 361-379 (in Japanese).

5) Barber, N. F.: The Directional Resolving Power of an Array of Wave Detectors, Proc. Ocean Wave Spectra Prentice Hall, 1963, pp. 137-160.

6) Panicker, N. N. and L. E. Borgman: Directional Spectrum from Wave Gauge Arrays, Proc. 12th Conf. on Coastal Engg., Washington, 1970, pp. 117-136.

7) Panicker, N. N.: Determination of Directional Spectra of Ocean Wave from Gauge Array, Tech. Report, HEL 1-18, Hydr. Engg. Lab., Univ. of California, 1971, pp. 1-315.

8) Chakrabarti, S. K. and R. H. Snider: Design of Wave Staff for Directional Wave Energy Distribution, Underwater Journal, Vol. 5, No. 5, 1972, pp. 200-208.

9) Chakrabarti, S. K. and R. H. Snider: Two-Dimensional Wave Energy Spectra, Underwater Journal, Vol. 2, 1973, pp. 80-85.

10) Fan, S. S.: Diffraction of Wind Waves, Tech. Report, HEL 1-10, Hydr. Engg. Lab., Univ. of California, 1968, pp. 1-156.

11) Suzuki, Y.: Observation of Approximate Directional Spectra for Coastal Waves, Proc. 16th Conf. on Coastal Engg., 1966, pp. 99-106 (in Japanese).

12) Fujinawa, Y.: Measurement of Directional Spectrum of Wind Waves Using an Array of Wave Detectors, Part 1; A New Technique of Evaluation, Jour. Oceanogr. Soc. Japan, Vol. 30, 1974, pp. 10-22.

13) Borgman, L. E.: Directional Spectra Model for Design Use, Tech. Report, HEL 1-12, Hydr. Engg. Lab., Univ. of California, 1969, pp. 1-29.

14) Horiguchi, T.: An Approach to Directional Spreading of Waves, Proc. 12th Conf. on Coastal Engg., 1968, pp. 64-68 (in Japanese).

15) Mobarek, I.: Directional Spectra of Laboratory Wind Waves, Proc. ASCE, Jour. Waterways and Harbour Div., Vol. 91, No. WW3, 1965, pp. 91-119.

16) Borgman, L. E.: Ocean Wave Simulation for Engineering Design, Tech. Report, HEL 9-13, Hydr. Engg. Lab., Univ. of California, 1967, pp. 1-57.

17) Goda, Y.: Numerical Experiments on Wave Statistics with Spectral Simulation, Report, Port and Harbour Res. Inst., Vol. 9, No. 3, 1970, pp. 1-57.

18) Iwagaki, Y. and A. Kimura: Study on Simulation Method of Ocean Waves with an Arbitrary Spectral Shape, Proc. 20th Conf. on Coastal Engg., 1973, pp. 463-467 (in Japanese).

19) Hasselmann et al.: Measurements of Wind Wave Growth and Swell Decay During the Joint North Sea Wave Project (JONSWAP), Ergänzungsheft zur Deutschen Hydrographischen Zeitschrift, Reihe A, Nr. 12, 1973, pp. 1-95.

Wave Refraction and Wave Height
Variation Due to Current

By Yuichi IWAGAKI, Tetsuo SAKAI,
Toshio TSUDA and Yukio OKA

(Manuscript received June 10, 1977)

Abstract

This paper deals with the wave refraction due to current by a theoretical treatment and a numerical model. The theory of refraction of deep-water waves traversing a simple horizontal current with vertical axis of shear by Longuet-Higgins and Stewart[1] is extended to the case of shallow-water waves. It is found that the wave direction and wave height of shallow-water waves refracted by the current vary more rapidly than those of deep-water waves, and the variation of wave height is expressed as the product of the similar coefficients to the shoaling and refraction coefficients and a coefficient representing the effect of the radiation stress. A numerical model is presented for the wave refraction due to current. The variation of wave direction is calculated with the wave orthogonal equation along a path propagating in the direction of the sum of the wave velocity and the current, which is derived from the irrotational condition of wave number. The variation of wave height is also calculated with the equation of wave energy conservation in current derived by Longuet-Higgins and Stewart[1] along another path propagating in the direction of the sum of the group velocity and the current. The numerical results agree roughly with the theoretical results, and the validity of the numerical model is roughly confirmed. The effects of the relative wave velocity to the current, the derivatives of wave direction with respect to the horizontal coordinates and the radiation stress on the wave refraction due to current are found to be not negligible.

1. Introduction

Refraction of waves due to current is one of wave transformation phenomena. This phenomenon has not been investigated so widely compared with wave shoaling, wave refraction by underwater topography and wave diffraction.

Longuet-Higgins and Stewart[1] presented a wave energy conservation equation in current including the so-called radiation stress. They showed that the existing theoretical treatments[2]~[4] for the wave height variation of the refracted waves due to current failed to take the effect of this radiation stress into account. Taking the radiation stress into account, they solved the deep-water wave refraction due to current in special cases theoretically. They neglected the effect of the waves on the current.

In this paper, a theoretical treatment of the shallow-water wave refraction due to current in the same case as Longuet-Higgins and Stewart treated is presented. These theoretical results, however, can predict the wave refraction due to current only in special cases. A numerical model is necessary for the prediction of the wave refraction due to current of arbitrary distribution.

Recently, several theoretical models for the prediction of nearshore circulations due to waves in the surf zone have been presented[5]~[10]. These theories neglected the wave-current interaction as the first step to predict the nearshore circulation. Noda, Sonu, Rupert and Collins[11] and Skovgaard and Jonsson[12] presented independently numerical models for the prediction of the wave-current interaction. Noda et al. made use of a kinematic conservation equation of waves in current by Phillips[13] and the dynamic conservation equation of wave energy in current by Longuet-Higgins and Stewart[1]. They repeated the computation of the current induced by the waves and the computation of the wave refraction due to the current alternately to take the effects of the wave-current interaction on the nearshore circulation into consideration. Skovgaard and Jonsson made use of a wave energy conservation equation of different type from that by Longuet-Higgins and Stewart which they called "the equation of wave action conservation".

A similar numerical model for prediction of wave refraction due to current is presented here. The same two equations as Noda et al. used are applied as the basic equations. The current, however, is assumed not to be affected by the waves in contrast to two models mentioned above. The wave direction is calculated by a technique of integrating along characteristic lines similar to the conventional numerical technique of the wave refraction by underwater topography[14]. The wave height is also calculated by the technique of integrating along characteristic lines different from those mentioned above.

This numerical model is applied to special cases which are able to be predicted by the theoretical treatment. The numerical results are compared with the theoretical ones, and the validity of the numerical model is discussed. The effects of the relative wave celerity, the derivatives of wave direction and the radiation stress are also discussed with the numerical results.

2. Theoretical Treatment of Wave Refraction Due to Current

2.1 Deep-water wave refraction due to current[1]

Longuet-Higgins and Stewart[1] treated a case of waves traversing a simple horizontal current with vertical axis of shear. The stream velocity $(U, 0, 0)$ is supposed to be everywhere parallel to the x-axis and also

$$\partial U/\partial x = \partial U/\partial z = 0. \qquad (1)$$

The angle of the wave direction with the x-axis is denoted by θ (Fig. 1). It is assumed that the range of value of θ is $0° \sim 90°$ and U takes both positive and negative values. The wave number k is irrotational due to the definition of the wave number (Phillips[13]), that is,

$$\partial k_x/\partial y - \partial k_y/\partial x = 0, \qquad (2)$$

where k_x and k_y are the x- and y-components of k. Since the current varies only in the y-direction, the wave length and wave height are independent of x. Furthermore,
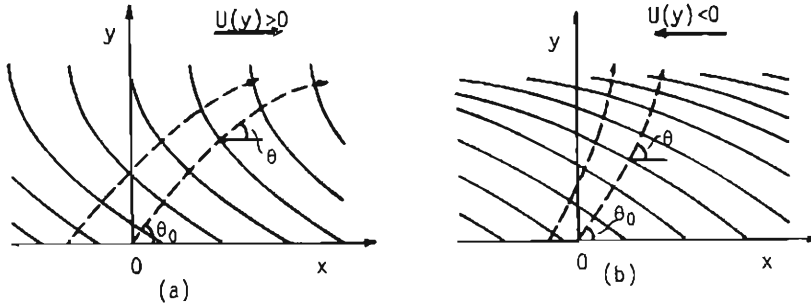
Fig. 1. Definition diagram for waves on a shearing current.

the wave number in the x-direction is $k \cos \theta$. So, we have

$$k \cdot \cos \theta = \text{const.} = b. \tag{3}$$

The kinematic conservation equation for the wave number given by Phillips is as follows:

$$\partial k / \partial t + \nabla \omega = 0, \tag{4}$$

where ω is the apparent angular frequency of the waves relative to a fixed point. Since the apparent velocity of the waves at right-angles normal to their crests is $(c_* + U \cos \theta)$ and their wave number is k, the apparent angular frequency ω of the waves is $k(c_* + U \cos \theta)$. Therefore, considering the steady state, equation (4) becomes

$$k(c_* + U \cos \theta) = \sigma_0, \tag{5}$$

where c_* is the relative wave velocity to the current in the presence of current and σ_0 the angular frequency of the waves in the region of no current. Thirdly, we have the relation connecting the local wave number and the relative wave velocity in deep-water waves:

$$k \cdot c_*^2 = g. \tag{6}$$

Equation (6) is applicable if the water depth and the current vary slowly. From equations (3), (5) and (6), we have

$$c_*/c_0 = 1/(1 - U/c_0 \cdot \cos \theta_0), \tag{7}$$
$$k/k_0 = (1 - U/c_0 \cdot \cos \theta_0)^2, \tag{8}$$
$$\cos \theta / \cos \theta_0 = 1/(1 - U/c_0 \cdot \cos \theta_0)^2, \tag{9}$$

where c_0, k_0 and θ_0 denote the values of c, k and θ in the region of no current. It should be noticed that in general c_0, k_0 and θ_0 are not the values in deep water but in this case they are equal to the values in deep water.

The refracted wave height variation in the current is calculated by using the wave energy conservation equation in current[1]:

$$\partial E/\partial t + \partial\{E(U + c_{g*x})\}/\partial x + \partial\{E(V + c_{g*y})\}/\partial y$$
$$+ S_{xx} \cdot \partial U/\partial x + S_{xy} \cdot \partial V/\partial x + S_{yx} \cdot \partial U/\partial y + S_{yy} \cdot \partial V/\partial y = 0. \tag{10}$$

S is the so-called radiation stress and given as follows:

$$S = E \left\{ \begin{array}{ll} \dfrac{c_{g*}}{c_*}\cos^2\theta + \dfrac{1}{2}\left(\dfrac{2c_{g*}}{c_*} - 1\right), & \dfrac{c_{g*}}{c_*}\cos\theta \cdot \sin\theta \\[3mm] \dfrac{c_{g*}}{c_*}\cos\theta \cdot \sin\theta, & \dfrac{c_{g*}}{c_*}\sin^2\theta + \dfrac{1}{2}\left(\dfrac{2c_{g*}}{c_*} - 1\right) \end{array} \right\}, \tag{11}$$

where c_{g*} is the relative group velocity of the waves to the current, c_{g*x} and c_{g*y} the x- and y-components of c_{g*} and E the wave energy. Johnson[3] considered the same case without taking into account the radiation stress. The group velocity in deep water is given by $1/2 \cdot c_*$. Hence equation (10) becomes in the steady state, eliminating all derivatives with respect to t and x,

$$\partial(E \cdot 1/2 \cdot c_*\sin\theta)/\partial y + 1/2 \cdot E\partial U/\partial y \cdot \cos\theta\sin\theta = 0. \tag{12}$$

On substitution from equations (7)~(9), the integral of equation (12) gives

$$E \cdot \sin\theta / (\sigma_0 - bU)^2 = \text{const.} \tag{13}$$

or, from equation (9),

$$E \cdot \sin 2\theta = \text{const.} \tag{14}$$

The relative amplification of the waves is therefore given by

$$H/H_0 = (E/E_0)^{\frac{1}{2}} = (\sin 2\theta_0/\sin 2\theta)^{\frac{1}{2}}, \tag{15}$$

where H and H_0 are the wave heights in the regions of current and no current respectively.

2.2 Shallow-water wave refraction due to current

As seen from equation (8), the wave length becomes longer than that in the region of no current when the current is in the positive x-direction. Hence the situation in which the relative wave velocity is given by equation (6) may be limited. Here the relation between the relative wave velocity and the local wave number is assumed to be given by the shallow-water wave relation of small amplitude waves:

$$k \cdot c_*^2 = g \cdot \tanh kh, \tag{16}$$

where h is the water depth. Equations (3) and (5) are applicable also in this case. In the same manner as in 2.1, we have

$$c_*/c_0 = 1/(1 - U/c_0 \cdot \cos\theta_0) \cdot \tanh kh/\tanh k_0 h_0, \tag{17}$$

$$k/k_0 = (1 - U/c_0 \cdot \cos\theta_0)^2 \cdot \tanh k_0 h_0/\tanh kh, \tag{18}$$

$$\cos\theta/\cos\theta_0 = 1/(1 - U/c_0 \cdot \cos\theta_0)^2 \cdot \tanh kh/\tanh k_0 h_0, \tag{19}$$

where h_0 is the water depth in the region of no current $(y < 0)$. It is evident that

in this case the terms underlined are added to equations $(7) \sim (9)$ in the case of deep-water wave refraction. As seen from equation (18), the unknown k is included in both left and right hand sides. So it is necessary to calculate the value of k by iteration.

The relative group velocity is given by

$$c_{g*}/c_* = n_* = 1/2 \cdot (1 + 2\,kh/\sinh 2kh). \tag{20}$$

Using equation (20), equation (10) becomes in this case

$$\frac{\partial}{\partial y}\left(\frac{n_* \cdot E \cdot \tanh kh \cdot \sin\theta}{\sigma_0 - bU} \right) + n_* \frac{E \cdot b \cdot \tanh kh \cdot \sin\theta}{(\sigma_0 - bU)^2} \frac{\partial U}{\partial y} = 0. \tag{21}$$

The integral of equation (21) gives

$$n_* \cdot E \cdot \tanh kh \cdot \sin\theta / (\sigma_0 - bU)^2 = \text{const.,} \tag{22}$$

or, from equation (19),

$$n_* \cdot E \cdot \sin 2\theta = \text{const.} \tag{23}$$

The relative amplification of the waves is therefore given by

$$H/H_0 = (E/E_0)^{\frac{1}{2}} = (\sin 2\theta_0/\sin 2\theta)^{\frac{1}{2}} \cdot (n_0/n_*)^{\frac{1}{2}}, \tag{24}$$

where n_0 is n in the region of no current.

Since $\cos\theta$ in equation (19) can not exceed unity, there is clearly an upper limit to U for which a solution exists:

$$U/c_0 \leq \{1 - (\cos\theta_0 \cdot \tanh kh/\tanh k_0 h_0)^{\frac{1}{2}}\}/\cos\theta_0. \tag{25}$$

It is evident that in the case of deep-water wave refraction the term underlined in equation (25) is equal to unity. At this upper limit θ becomes equal to 0, and the waves are interrupted to proceed by the current. On the other hand, for negative current $U < 0$, there is no kinematic limit to U. However, as $U \to -\infty$, k becomes very large, that is to say, the wave length becomes very small (Fig. 1, (b)). The angle θ approaches $90°$, that is, the direction of propagation becomes nearly normal to the current. Fig. 2 shows the variations of the wave direction. The broken line curves are for the deep-water wave refraction (equation (9)). The full line curves are examples for the shallow-water wave refraction ($k_0 h_0 = 0.1$ in equation (19)). It is evident that in the shallow-water wave refraction the wave direction varies more rapidly than in the deep-water wave refraction.

As seen from equations (15) and (24), the wave height becomes infinite both when $\theta \to 0°$ and $\theta \to 90°$. Longuet-Higgins and Stewart[1] described on this phenomenon as follows:

In the first case the infinity is not significant: it is due to the fact that the ray-paths intersect, and the corresponding line $y = $ const. is a caustic.
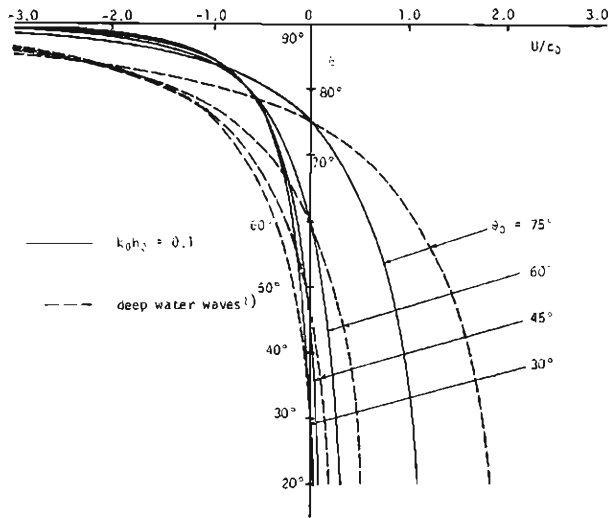
Fig. 2. Variation of direction of waves crossing a shearing current
at an oblique angle θ for various initial angles θ_0

In the neighbourhood of such a line the ordinary approximations of ray optics
do not apply; a higher-order theory, generally involving Airy functions, must
be used. One may expect that the wave amplitude in fact remains finite
even in the neighbourhood of the critical line.

The second case, when $\theta \rightarrow 90°$, corresponds to the limit $U \rightarrow -\infty$. In that
case the infinity is genuine and is due mainly to the fact that the wave
length and wave velocity are so much reduced that, in order to maintain the
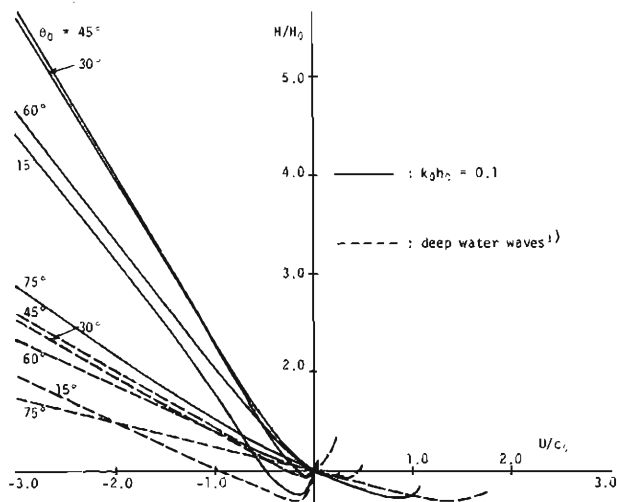

Fig. 3. Variation of height of waves crossing a shearing current
at an oblique angle for various initial angles θ_0

energy flux in the y-direction, the wave height must increase. In practice the waves may break; but for no finite velocity $U < 0$ is the ratio H/H_0 theoretically infinite.

We may note that it is possible for the component of stream velocity opposite to the waves to exceed the group velocity:

$$1/2 \cdot c_* + U \cos \theta < 0.$$

The waves are not thereby stopped, for the wave amplitude tends to be diminished by a lateral stretching of the wave crests.

Fig. 3 shows the variations of the wave height H. The broken line curves are for the deep-water wave refraction (equation (15)), and the full line curves are examples for the shallow-water wave refraction ($k_0 h_0 = 0.1$ in equation (24)). It is evident that in the shallow-water wave refraction the wave height varies more rapidly than in the deep-water wave refraction.

2.3 Effect of radiation stress

Dividing equation (19) by equation (17) yields

$$\cos \theta / \cos \theta_0 = (c_*/c_0)/(1 - U/c_0 \cdot \cos \theta_0). \tag{26}$$

Substituting equation (26), equation (24) becomes

$$H/H_0 = (n_0 c_0/n_* c_*)^{\frac{1}{2}} \cdot (\sin \theta_0/\sin \theta)^{\frac{1}{2}} \cdot (1 - U/c_0 \cdot \cos \theta_0)^{\frac{1}{2}}. \tag{27}$$

If the deep-water wave velocity without current c_d is used as c_0, $n_0 = n_d = 1/2$ and equation (27) becomes

$$H/H_d = K_s' \cdot K_r' \cdot K_{rs}, \tag{28}$$
$$K_s' = (c_d/2 \, n_* c_*)^{\frac{1}{2}}, \tag{29}$$
$$K_r' = (\sin \theta_d/\sin \theta)^{\frac{1}{2}}, \tag{30}$$
$$K_{rs} = (1 - U/c_d \cdot \cos \theta_d)^{\frac{1}{2}}. \tag{31}$$

The coefficient K_s' has the same form as the shoaling coefficient K_s except for that n and c are replaced with n_* and c_*. This coefficient means the rate of wave height variation due to not only the water depth variation but also the current. The coefficient K_r' has the same form as the refraction coefficient K_r. The wave direction θ is however the refracted wave direction not only by the underwater topography but also due to the current. If the radiation stress is neglected in equation (21), it will be found that

$$H/H_d = K_s' \cdot K_r'. \tag{32}$$

The coefficient K_{rs} therefore represents the effect of the radiation stress on the wave height variation. In equation (31), $\cos \theta_d$ is positive for $0° < \theta_d < 90°$. Therefore if $U > 0$, that is, the current is in the same direction of the waves, $K_{rs} < 1$ so that the wave height is damped. On the contrary, if $U < 0$, that is, the current is in the

opposite direction to the waves, $K_{rs}>1$ so that the wave height is amplified.

3. Numerical Model of Wave Refraction Due to Current

3.1 Wave orthogonal equation

In the theoretical treatment, the wave direction θ is determined with the irrotational condition of the wave number (equation (2)). On the other hand, in the conventional numerical technique for wave refraction by underwater topography[14], the wave direction is determined by the equation of the curvature of a ray along the ray. A similar equation is derived by Arthur[15] for the wave refraction due to current.

$$d\theta/dt = \partial(q_c + c_*)/\partial x \cdot \sin\theta - \partial(q_c + c_*)/\partial y \cdot \cos\theta, \qquad (33)$$

$$dx/dt = U + c_* \cos\theta, \quad dy/dt = V + c_* \sin\theta, \qquad (34)$$

where x and y are the horizontal coordinates, U and V are x- and y- components of the current and q_c is the component of the current in the direction of c_* as shown in Fig. 4:

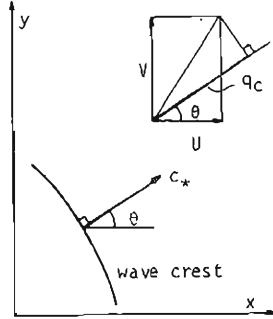$$q_c = U\cos\theta + V\sin\theta. \qquad (35)$$

Fig. 4. Definition diagram for numerical model of wave refraction due to current.

The above equations mean that the variation of the wave direction θ with time along a path given by equation (34) is represented by equation (33). Skovgaard and Jonsson[12] called equation (33) "wave orthogonal equation".

A similar equation is also derived from the irrotational condition of wave number (equation (2)). Using the relationships $k_x = k\cos\theta$ and $k_y = k\sin\theta$, equation (2) is transformed as

$$\cos\theta \cdot \partial\theta/\partial x + \sin\theta \cdot \partial\theta/\partial y = \cos\theta/k \cdot \partial k/\partial y - \sin\theta/k \cdot \partial k/\partial x. \qquad (36)$$

The kinematic conservation equation of waves (4) is given in this two-dimensional

case as

$$k(c_* + U\cos\theta + V\sin\theta) = \sigma_0. \tag{37}$$

Differentiating equation (37) yields

$$\frac{\partial k}{\partial x} = \frac{-\sigma_0\left\{\dfrac{\partial c_*}{\partial x} + \dfrac{\partial U}{\partial x}\cos\theta + \dfrac{\partial V}{\partial x}\sin\theta + \dfrac{\partial\theta}{\partial x}(-U\sin\theta + V\cos\theta)\right\}}{(c_* + U\cos\theta + V\sin\theta)^2} \tag{38}$$

and

$$\frac{\partial k}{\partial y} = \frac{-\sigma_0\left\{\dfrac{\partial c_*}{\partial y} + \dfrac{\partial U}{\partial y}\cos\theta + \dfrac{\partial V}{\partial y}\sin\theta + \dfrac{\partial\theta}{\partial y}(-U\sin\theta + V\cos\theta)\right\}}{(c_* + U\cos\theta + V\sin\theta)^2}. \tag{39}$$

Substituting equations $(37)\sim(39)$, equation (36) becomes

$$\frac{\partial\theta}{\partial x}(U + c_*\cos\theta) + \frac{\partial\theta}{\partial y}(V + c_*\sin\theta)$$

$$= \left(-\frac{\partial U}{\partial y}\cos\theta + \frac{\partial U}{\partial x}\sin\theta\right)\cos\theta + \left(-\frac{\partial V}{\partial y}\cos\theta + \frac{\partial V}{\partial x}\sin\theta\right)\sin\theta$$

$$+ \left(-\frac{\partial c_*}{\partial y}\cos\theta + \frac{\partial c_*}{\partial x}\sin\theta\right). \tag{40}$$

The rate of variation with time along the path given by equation (34) is written as

$$\frac{d}{dt} = \frac{\partial}{\partial t} + \frac{dx}{dt}\frac{\partial}{\partial x} + \frac{dy}{dt}\frac{\partial}{\partial y} = (U + c_*\cos\theta)\frac{\partial}{\partial x} + (V + c_*\sin\theta)\frac{\partial}{\partial y} \tag{41}$$

in the steady state. Equation (40) is therefore expressed as follows:

$$\frac{d\theta}{dt} = \left(-\frac{\partial U}{\partial y}\cos\theta + \frac{\partial U}{\partial x}\sin\theta\right)\cos\theta + \left(-\frac{\partial V}{\partial y}\cos\theta + \frac{\partial V}{\partial x}\sin\theta\right)\sin\theta$$

$$+ \left(-\frac{\partial c_*}{\partial y}\cos\theta + \frac{\partial c_*}{\partial x}\sin\theta\right). \tag{42}$$

On the other hand, equation (33), substituting equation (35), becomes

$$\frac{d\theta}{dt} = \left(-\frac{\partial U}{\partial y}\cos\theta + \frac{\partial U}{\partial x}\sin\theta\right)\cos\theta + \left(-\frac{\partial V}{\partial y}\cos\theta + \frac{\partial V}{\partial x}\sin\theta\right)\sin\theta$$

$$+ \left(-U\sin^2\theta + V\sin\theta\cdot\cos\theta\right)\frac{\partial\theta}{\partial x} + \left(-V\cos^2\theta + U\sin\theta\cdot\cos\theta\right)\frac{\partial\theta}{\partial y}$$

$$+ \left(-\frac{\partial c_*}{\partial y}\cos\theta + \frac{\partial c_*}{\partial x}\sin\theta\right). \tag{43}$$

It is evident that equation (43) has the additional terms containing $\partial\theta/\partial x$ and $\partial\theta/\partial y$ compared with equation (42). This discrepancy is not discussed here. Equations (42) and (34) derived from the irrotational condition of wave number are used in this numerical model.

Noda et al.[11] used equation (36) giving the irrotational condition of wave number, but they solved equation (36) directly on the numerical grid points instead of using the technique of integrating along the path given by equation (34).

3.2 Relative wave velocity to current

As mentioned above, the kinematic conservation equation of waves in current is represented as follows :

$$k(c_* + U\cos\theta + V\sin\theta) = \sigma_0 = 2\pi/T, \tag{44}$$

where T is the period of waves in the region of no current. On the other hand, equation (16) is assumed as the relation between the relative wave velocity to current and the local wave number. Combining equations (44) and (16), we have

$$L_* \equiv \frac{2\pi}{k} = \frac{gT^2/2\pi \cdot \tanh(2\pi h/L_*)}{(1 - T/L_* \cdot U\cos\theta - T/L_* \cdot V\sin\theta)^2}. \tag{45}$$

Therefore if the wave period T, the water depth h, two components of current velocity U and V and the wave direction θ are known, the wave length L_* is determined by iteration. Then the relative wave velocity c_* is obtained from equation (16). The characteristics of the wave length in current was discussed in detail by Jonsson, Skovgaard and Wang[16].

3.3 Wave energy equation

The wave energy conservation equation in current (10) derived by Longuet-Higgins and Stewart[1] is used here. Considering the steady state and the representation of the radiation stress (11), equation (10) becomes

$$(U + c_{g*}\cos\theta)\frac{\partial E}{\partial x} + (V + c_{g*}\sin\theta)\frac{\partial E}{\partial y} = F(U, V, c_*, c_{g*}, \theta) \cdot E, \tag{46}$$

where

$$\begin{aligned}
F = &-\frac{\partial U}{\partial x} + \frac{\partial V}{\partial y} + \frac{\partial c_{g*}}{\partial x}\cos\theta + \frac{\partial c_{g*}}{\partial y}\sin\theta + c_{g*}\left(-\sin\theta\frac{\partial\theta}{\partial x} + \cos\theta\frac{\partial\theta}{\partial y}\right) \\
&+ \left\{\frac{c_{g*}}{c_*}\cos^2\theta + \frac{1}{2}\left(\frac{2c_{g*}}{c_*} - 1\right)\right\}\frac{\partial U}{\partial x} + \frac{c_{g*}}{c_*}\cos\theta \cdot \sin\theta\left(\frac{\partial V}{\partial x} + \frac{\partial U}{\partial y}\right) \\
&+ \left\{\frac{c_{g*}}{c_*}\sin^2\theta + \frac{1}{2}\left(\frac{2c_{g*}}{c_*} - 1\right)\right\}\frac{\partial V}{\partial y}. \tag{47}
\end{aligned}$$

Lets consider a path given by

$$dx/dt = U + c_{g*}\cos\theta, \quad dy/dt = V + c_{g*}\sin\theta. \tag{48}$$

Along this path, the rate of wave energy variation with time is, from equation (46), given as

$$dE/dt = F(U, V, c_*, c_{g*}, \theta) \cdot E. \tag{49}$$

This representation of the wave energy variation is similar to that of the wave direction variation (42) and (34). Two paths given by equations (34) and (48) do not coincide, for c_{g*} is not equal to c_* in general. Furthermore, the term F contains the wave direction θ. So, before the calculation of the wave energy variation, it is necessary to calculate the wave direction variation by using equations (42) and (34).

In the conventional numerical technique of wave refraction by underwater topography[4], the refraction coefficient is calculated at each step point along a ray according to the theory developed by Munk and Arthur[7]. It is clear that the calculation of the wave height in wave refraction due to current is not so simple compared with the calculation in wave refraction by underwater topography only.

Noda et al. solved equation (46) directly on the numerical grid points. In this numerical model, equations (48) and (49) are used. The wave height H is calculated with the relationship $E = 1/8 \cdot \rho g H^2$.

3.4 Numerical computation

The region of computation is constructed by a set of perpendicular grids of equal spacing Δs (Fig. 5). At each grid point, the water depth h, two components of current velocity U and V are known. On the offshore boundary $j=1$, the initial wave direction θ_0 and the initial wave height H_0 are known. The wave period T is given and constant in the whole region. The numerical computation consists of two parts. In the first part, the wave direction θ is calculated by using equations (42) and (34). After that, the wave height H is calculated by using the calculated values of wave direction and the equations (48) and (49).

The path in the calculation of wave direction given by equation (34) starts at each grid point on the offshore boundary $j=1$. Along each path, the new step point (x_m, y_m) and the wave direction θ_m are calculated every time increment Δt (Fig. 6). In practice, at each step, the temporary increment of θ (denoted by $\Delta\theta_m'$) is calculated
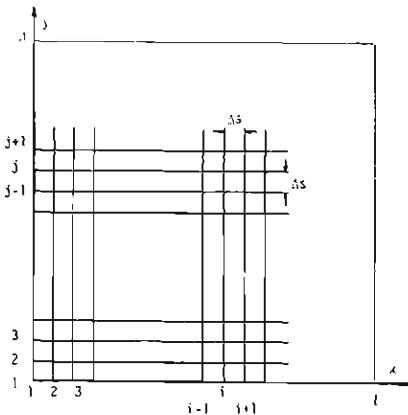

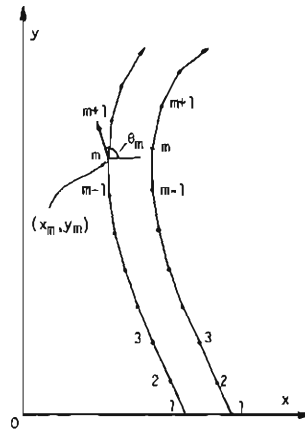Fig. 5. Set of perpendicular grids of equal spacing Δs.

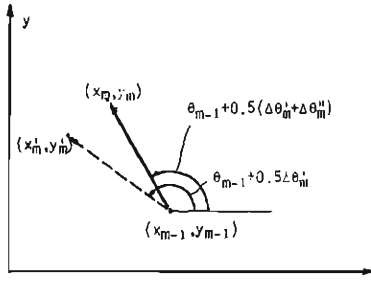Fig. 6. Paths in calculation of wave direction.
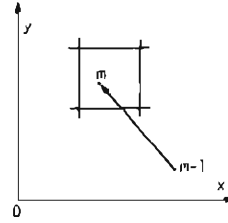
Fig. 7. Temporary step point.

Fig. 8 Interpolation from values on four grid
points surrounding a step point

at first (Fig. 7). The temporary step point (x_m', y_m') is calculated by the equations

$$x_m' = x_{m-1} + c_{*m-1} \cdot \cos(\theta_{m-1} + 1/2 \cdot \Delta\theta_m') \cdot \Delta t + U_{m-1} \cdot \Delta t, \tag{50}$$

$$y_m' = y_{m-1} + c_{*m-1} \cdot \sin(\theta_{m-1} + 1/2 \cdot \Delta\theta_m') \cdot \Delta t + V_{m-1} \cdot \Delta t. \tag{51}$$

At this temporary point, the increment of θ (denoted by $\Delta\theta_m''$) is calculated again. The final new wave direction and the new step point are calculated by the equations

$$\theta_m = \theta_{m-1} + 1/2 \cdot (\Delta\theta_m' + \Delta\theta_m''), \tag{52}$$

$$x_m = x_{m-1} + c_{*m-1} \cdot \cos\theta_m \cdot \Delta t + U_{m-1} \cdot \Delta t, \tag{53}$$

$$y_m = y_{m-1} + c_{*m-1} \cdot \sin\theta_m \cdot \Delta t + V_{m-1} \cdot \Delta t. \tag{54}$$

In general, the step point does not coincide with the grid point (Fig. 8). In the calculation of equations (42) and (34), the interpolated value from the values on four grid points surrounding the step point is used. The derivatives of U, V and c_* with respect to x and y are also calculated from the values on four grid points.

The calculation of wave direction along each path is stopped if the path runs out of the boundary of the computation region. Therefore, in general, some part of the computation region is left in which the value of wave direction is not calculated
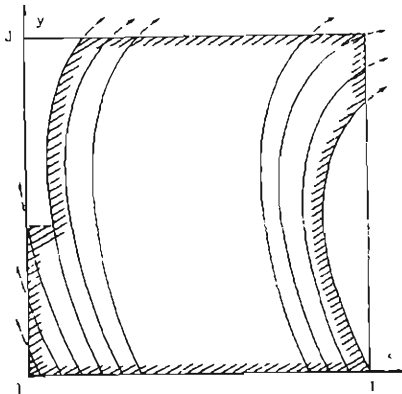

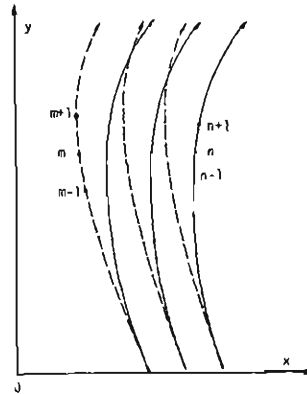Fig. 9. Region in which wave directions
are calculated.

Fig. 10. Paths in calculation of wave height.

(Fig. 9). The values of θ on the grid points are interpolated from the calculated values of θ on the nearest three step points for the next calculation of wave height.

The path in the calculation of wave height given by equation (48) also starts at each grid point on the offshore boundary $j=1$. Along each path, the new step point (x_n, y_n) and new wave height H_n are calculated every time increment Δt by using equation (49) (Fig. 10). In the wave height calculation, the temporary step point used in the wave direction calculation is not used. In the same manner as in the wave direction calculation, the values and derivatives at the step point are interpolated from the values on four grid points surrounding the step point. The calculation of wave height along each path is stopped if the path runs out of the region where the interpolated values of wave direction are registered on the grid points.

As an example of the numerical computation, a $500 \, \text{m} \times 500 \, \text{m}$ rectangular region with a simple current of only the x-component of velocity U increasing linearly in the y-direction (Fig. 11) is considered.

$$U = \begin{cases} 0 : 0 \leq y \leq 80 \text{ m}, \\ 0.01 (y-80) \text{ m/s} : 80 \text{ m} \leq y \leq 500 \text{ m}. \end{cases} \tag{55}$$

The cases of constant water depth and plane beach are considered. In the case of plane beach the water depth decreases in the y-direction and becomes 0 at $y=500$ m. The grid spacing Δs is set equal to 20 m, and the wave period T is 5 sec. The time increment Δt is set equal to $1/2 \cdot T$. In the numerical model, the current U takes only positive value, and the wave direction θ can vary from $0°$ to $180°$. The numerical results for $\theta_0 > 90°$ are comparable with the theoretical results for the initial wave direction of $\theta_0 - 90°$ and the current $-U$. The initial wave height H_0 is 1m.
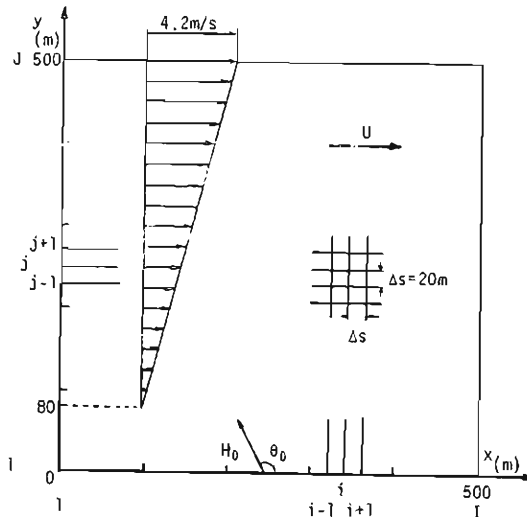

Fig. 11. 500m×500m rectangular region with a simple current of only x-component of velocity U increasing linearly in y-direction.

4. Results of Numerical Computation and Discussions

4.1 Comparisons of numerical and theoretical results

Fig 12 shows an example of comparisons of the numerical and theoretical results for the cases of plane beach without current. In this case, the slope of beach is 1/50. At the offshore boundary $y=0$ the water depth is 10 m and the initial wave direction θ_0 is 135° (Fig. 11). The theoretical values are calculated by using equations (19) and (24). The numerical results agree well with the theoretical results, and they show the well known behaviours that the wave direction becomes normal to the beach and the wave height decreases at first and increases as the waves approach the shoreline.

Fig. 13 shows the result of the case of uniform depth $h=30$m and the current given by equation (55). The initial direction of waves θ_0 is 60°, and the current is in the same direction of the waves. The numerical and theoretical results agree roughly. The wave direction becomes parallel to the direction of current gradually and the wave height decreases with increase in y. The theoretical curve of wave height increases after the initial decrease. This increase is not significant as described in the theoretical treatment. The numerical result does not exist in the range of the theoretical increase of wave height, because all paths run out of the boundary of computation region before approaching the boundary $y=500$m.

Fig. 14 shows the result of the same case as in Fig. 13 except for $\theta_0=120°$. The current is in the opposite direction to the waves. The numerical and theoretical results agree roughly also in this case. The wave direction becomes normal to the direction of the current gradually and the wave height increases with increase in y.

Fig. 15 shows the result of the same case as in Fig. 14 except for the uniform water depth $h=10$m. The numerical and theoretical results agree roughly. Compared
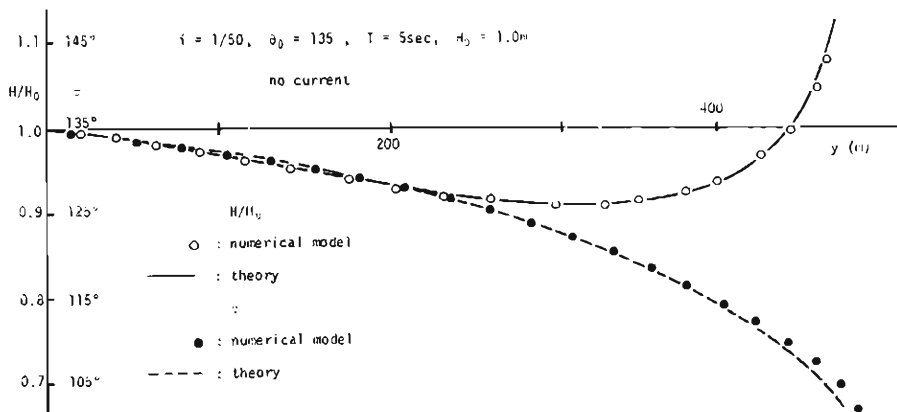

Fig. 12. Comparison between numerical and theoretical results for case of plane beach without current (beach slope=1/50, $\theta_0=135°$).
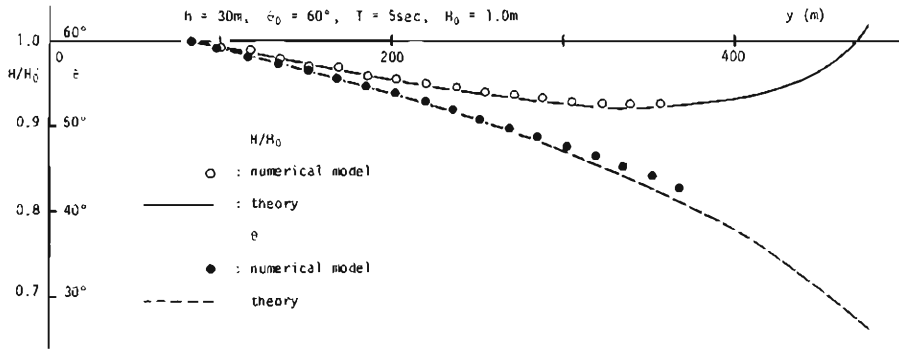
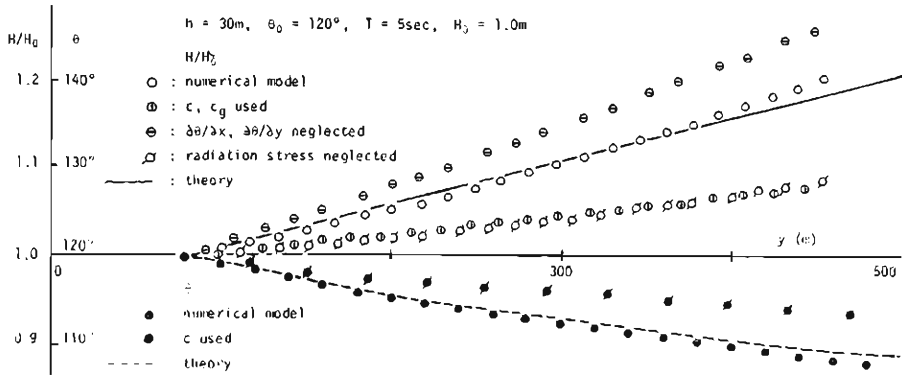Fig. 13. Comparison between numerical and theoretical results for case of uniform depth ($h=30$ m, $\theta_0=60°$).

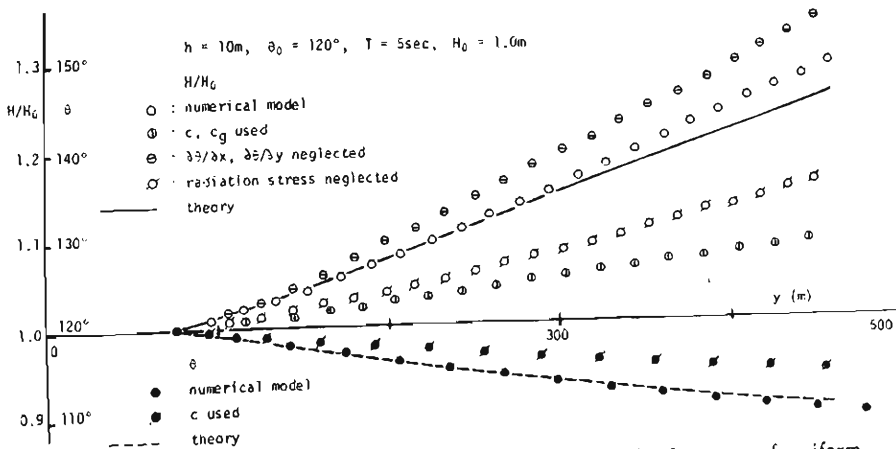Fig. 14. Comparison between numerical and theoretical results for case of uniform depth ($h=30$ m, $\theta_0=120°$).

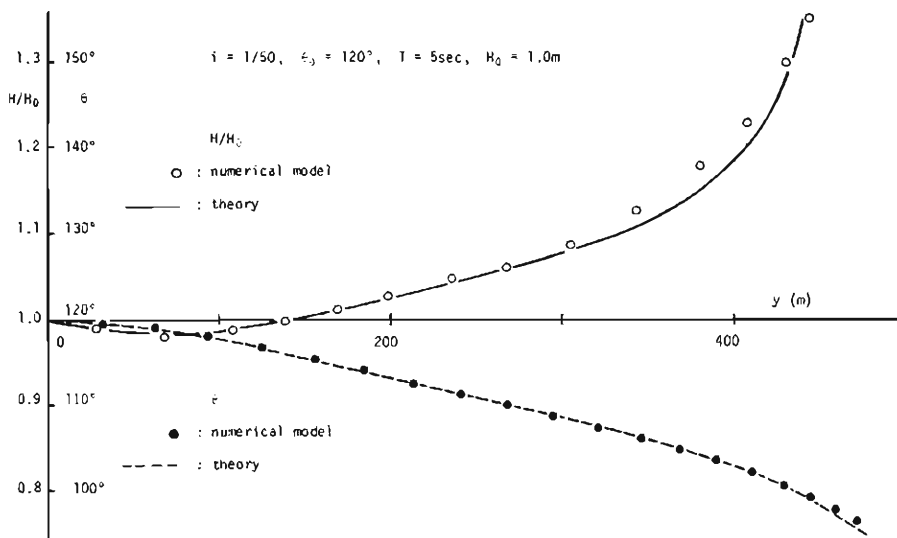Fig. 15. Comparison between numerical and theoretical results for case of uniform depth ($h=10$ m, $\theta_0=120°$).

Fig. 16. Comparison between numerical and theoretical results for case of plane beach (beach slope=1/50, $\theta_0 = 120°$).

with Fig. 14, the variations of wave direction and wave height for $h=10$ m resemble the variations for $h=30$ m. The rate of increase of wave height for $h=10$ m is however larger than that for $h=30$m. Also the differences between the numerical and theoretical results of wave height for $h=10$m are larger than those for $h=30$ m.

Fig. 16 shows an example of the results of the cases of plane beach and current. The slope of beach is 1/50 which is the same as the case of no current (Fig. 12). The initial wave direction is 120°. The numerical and theoretical results also agree roughly. As well as the case of Fig. 12, the wave direction becomes normal to the direction of the current gradually due to the underwater topography and the opposite current. The wave height becomes larger than that in the case of Fig. 12, because the rate of wave height increase is amplified by the opposite current.

As seen from five examples in Figs. 12~16, the numerical results agree roughly with the theoretical results. The differences between them however increase with increase in y. This is because the errors at each step in the numerical computation accumulate as the paths go on in the region of computation.

4.2 Effects of c_* and c_{g*}, $\partial\theta/\partial x$ and $\partial\theta/\partial y$ and radiation stress

As seen from equation (45), the wave length in the presence of current L_* is not equal to the wave length of small amplitude waves in the absence of current L. The relative wave velocity to the current c_* and the relative group velocity to the current c_{g*} calculated by using equations (16) and (20) respectively are also not equal to c and c_g in the absence of current. The value of wave direction θ is necessary to be known before the calculation of the wave length L_* by using equation (45). And the wave direction θ is one of the unknowns to be determined by

the numerical computation. This is one of the reasons why the numerical computation of wave refraction due to current is complicated compared with the numerical computation of wave refraction by underwater topography. If it would be possible to use c and c_g instead of c_* and c_{g*}, the computation would become fairly simple. In Figs. 14 and 15, two examples of the comparisons between the numerical results using c, c_g and c_*, c_{g*} under the same conditions are shown. In these cases, the calculated values of wave direction by using c are about the half of the value by using c_*, and the values of wave height by using c and c_g are about 30% or 40% of the values by using c_* and c_{g*}. As seen from these examples, the relative wave velocity and group velocity to current c_* and c_{g*} have to be used in the computation of wave refraction due to current.

As mentioned in **3**, there are two kinds of wave orthogonal equations, (42) and (43). In this numerical model, equation (42) is used. The effects of the terms containing $\partial\theta/\partial x$ and $\partial\theta/\partial y$ in equation (43) are therefore not discussed. On the other hand, the term F in the equation of wave energy variation (49) also has a term containing $\partial\theta/\partial x$ and $\partial\theta/\partial y$ (equation (47)) :

$$c_{g*}(-\sin\theta\cdot\partial\theta/\partial x+\cos\theta\cdot\partial\theta/\partial y).$$

In Figs. 14 and 15, two examples of comparisons between the numerical results of wave height considering and neglecting the term containing $\partial\theta/\partial x$ and $\partial\theta/\partial y$ in F are shown. In these cases, the values neglecting the term are about 1.2 times as large as the values considering the term. The term containing $\partial\theta/\partial x$ and $\partial\theta/\partial y$ in F is therefore not negligible in the computation of wave height.

Finally, the effect of the radiation stress on the wave height variation is discussed. The last three terms in F

$$\{c_{g*}/c_*\cdot\cos^2\theta+1/2\cdot(2c_{g*}/c_*-1)\}\cdot\partial U/\partial x$$
$$+c_{g*}/c_*\cdot\cos\theta\cdot\sin\theta(\partial V/\partial x+\partial U/\partial y)$$
$$+\{c_{g*}/c_*\cdot\sin^2\theta+1/2\cdot(2c_{g*}/c_*-1)\}\cdot\partial V/\partial y$$

represent the effect of the radiation stress. In Figs. 14 and 15, two examples of comparisons between the results of wave height considering and neglecting those terms are shown. The calculated values of wave height neglecting those terms are about a half of the values considering the radiation stress. The effect of the radiation stress is therefore not negligible in the computation of wave height.

As described above, any of the effects of c_* and c_{g*}, $\partial\theta/\partial x$ and $\partial\theta/\partial y$ and the radiation stress is not negligible at least in the cases treated here. These discussions are however limited to the cases treated here. It is necessary to apply this numerical model to many cases of currents of various distributions for the discussion of general characteristics of these effects.

5. Conclusions

The wave refraction and the wave height variation due to current are discussed by

a theoretical treatment and a numerical model. The main conclusions are as follows:

1) The theory of refraction of deep-water waves traversing a simple horizontal current with vertical axis of shear by Longuet-Higgins and Stewart[1] is extended to the case of shallow-water waves. The wave direction and wave height of shallow-water waves refracted by the current vary more rapidly than those of deep-water waves.

2) The variation of wave height in this case is expressed as the product of the similar coefficients to the well known shoaling and refraction coefficients and a coefficient representing the effect of radiation stress.

3) The wave orthogonal equation for wave refraction due to current given by Arthur[15] has additional terms containing the derivatives of wave direction with respect to the horizontal coordinates compared with the equation derived from the irrotational condition of wave number.

4) A numerical model is presented for the wave refraction due to current. The effect of the waves on the current is neglected in this model. This model consists of two parts: the computation of wave direction and the computation of wave height. The variation of wave direction is calculated with the wave orthogonal equation derived from the irrotational condition of wave number, which represents the variation of wave direction with time along a path propagating in the direction of the sum of the wave velocity and the current. The variation of wave height is also calculated with the equation of wave energy conservation in current derived by Longuet-Higgins and Stewart[1], along another path propagating in the direction of the sum of the group velocity and the current.

5) The numerical results agree roughly with the theoretical results, and the validity of the numerical model is roughly confirmed

6) The effect of the relative wave velocity to the current is not negligible in the computation of wave refraction due to current. Also the effects of the derivatives of wave direction with respect to the horizontal coordinates and the radiation stress on the wave height variation are not negligible.

References

1) Longuet-Higgins, M. S. and R. W. Stewart: The changes in amplitude of short gravity waves on steady non-uniform currents, Jour. Fluid Mech., Vol. 10, 1961, pp. 529-549.

2) Unna, P. J. H.: Waves and tidal streams, Nature, Lond., Vol. 149, 1942, pp. 219-220.

3) Johnson, J. W.: The refraction of surface waves by currents, Trans. Amer. Geophys. Union, Vol. 28, 1947, pp. 867-874.

4) Evans, J. T.: Pneumatic and similar breakwater, Proc. Roy. Soc., A. 231, 1955, pp. 457-466.

5) Bowen, A. J.: The generation of longshore currents on a plane beach, Jour. Marine Res., Vol. 27, No. 2, 1969, pp. 206-215.

6) Thornton, E. B.: Variation of longshore current across the surf zone, Proc. 12th Conf. Coastal Eng., 1970, pp. 291-308.

7) Longuet-Higgins, M. S.: Longshore currents generated by obliquely incident sea waves, Parts 1 and 2, Jour Geophys. Res., Vol. 75, No. 33, 1970, pp. 6778-6801.

8) Arthur, R. S.: A note on the dynamics of rip currents, Jour. Geophys. Res., Vol 67, No. 7, 1962, pp. 2777-2779.

9) Bowen, A. J.: Rip currents, Part 1, Theoretical investigations, Jour. Geophys. Res., Vol 74, No. 23, 1969, pp. 5467-5478.

10) Bowen, A. J. and D. L. Inman: Rip currents, Part 2, Laboratory and field observations, Jour. Geophys. Res., Vo. 74, No. 23, 1969, pp. 5478-5490.

11) Noda, E. K., C. J. Sonu, V. C. Rupert and J. I. Collins: Nearshore circulations under sea breeze conditions and wave-current interactions in the surf zone, Tetra Tech. Rep. TC-P-72-149-4, AD 776643, 1974.

12) Skovgaard, O. and I. G. Jonsson: Current depth refraction using finite elements, Proc. 15th Conf. Coastal Eng., 1976, pp. 721-737.

13) Phillips, O. M.: The Dynamics of the Upper Ocean, Cambridge University Press, 1966, pp. 43-44.

14) Griswold, G. M.: Numerical calculation of wave refraction, Jour. Geophys. Res., Vol. 63, No. 6, 1963, pp. 1715-1723.

15) Arthur, R. S.: Refraction of shallow water waves: The combined effect of currents and underwater topography, Trans. Amer. Geophys. Union, Vol. 31, No. 4, 1950, pp. 549-552.

16) Jonsson, I. G., O. Skovgaard and J. D. Wang: Interaction between waves and currents, Proc. 12th Conf. Coastal Eng., 1970, pp. 489-507.

17) Munk, W. H. and R. S. Arthur: Wave intensity along a refracted ray, National Bureau of Standard, Circ. 521, Gravity Waves, 1952.

Statistical Search for Migrations of
Aftershock Sequences

By Masajiro IMOTO and Yoshimichi KISHIMOTO

(Manuscript received October 3, 1977)

Abstract

Aftershock sequences in Kuril of August 11, 1969 and June 17, 1973 are investigated by a statistical method. On the assumption of a unilateral propagation of aftershock activity, the direction of propagation is likely to be normal to the trench axis. On the basis of this result, time-space plots of other sequences in Kuril are examined. It is commonly observed that a quiescent area of aftershock activity originates at the epicenter of the main shock, and spreads seaward with time. The spreading velocity of a quiescent area is estimated at 8~16 km/day.

1. Introduction

For many years, many investigations have been done regarding aftershock phenomena, such as the frequency of aftershocks with time, Gutenberg-Richter's law (b values), seismicity maps, and so on. Recently, closer researches[1],[2] on seismicity maps have been made by more accurate data of hypocentral parameters. An aftershock area is considered to indicate the fracture zone of the main shock[3]. On this assumption, maps of aftershocks play important roles for determining fault geometries and other source parameters. Also, the location of the main shock with respect to the aftershock area gives a hint on faulting characteriscics.

Kellher et al.[4] examined aftershock areas of some large earthquakes at the trenches of the Pacific Ocean and the Caribbean Sea, and tried to forecast locations of large shallow earthquakes in near future. It was mentioned that epicenters of the main shocks tended to be located near the landward side of the aftershock area, and they inferred that during large thrust earthquakes ruptures initiate at some depth and propagate upward and seaward. We[5] also examined relations between epicenters of the large thrust earthquakes and their aftershock areas using more recent and accurate data. Generally speaking, samely as one of their conclusions, epicenters of the main shocks are situated landward. But strictly, this tendency seems to be somewhat different for different regions, that is, this tendency is prominent in Kurll and not in New Britain and New Hebrides.

Mogi[6] investigated development of aftershock areas of some great earthquakes which occurred in the Circum-Pacific Seismic Belt. Development of aftershock areas were seen during one year after main shocks. In the same paper, rapid propagations of aftershock activities were reported for the Alaskan Earthquake of March 28, 1964 and the Aleutian Earthquake of Marth 9, 1957. Ida[7] proposed a model of slow-moving

disturbance of deformation to interpret the observed propagation of earthquake foci and nonseismic creep. His analysis was based on an assumption that thin fault gouge participates in viscous slip. The viscosity of the gouge was estimated from observed propagation speed. Investigations on the aftershock migration might give some rheological information in the source region.

In this paper, we investigate migration phenomena of aftershock sequences particularly in Kuril. Because, in this region, the seismic activity is high, many sequences with recent and accurate data of hypocenters are available, and aftershock activity is characterized by its large scale.[8] As mentioned in our paper cited above,[5] the relation between the epicenter of a main shock and its aftershock area, which is considered to be a distinctive feature of thrust faults, also holds good. These characters of the Kuril region are adequate to examine the aftershock activity systematically.

2. Data

We selected the sequences in which magnitude of main shocks are greater than 7, and each of which consisted of many shocks. These main shocks are listed in Table 1 and plotted in Fig. 1. The data of hypocentral coordinates, origin times, and magnitudes are after NOAA Earthquake Data File and Earthquake Data Report.

Magnitude-frequency relations were examined for two sequences of October 1963 and August 1969 so as to see detection capability for these sequences. All
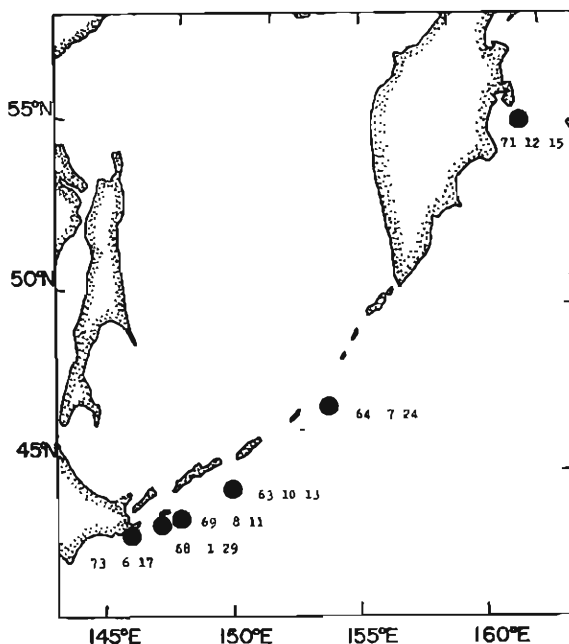

Fig. 1. Plots of the main shocks in Table 1.

Table 1. List of main shocks.

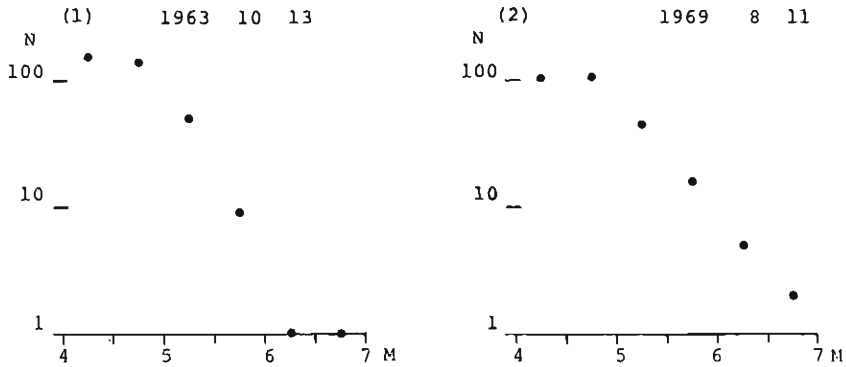|	Date		Origin Time			Epicenter		Depth	Mag.
Y	M	D	h	m	s	Lat.°N	Lon.°E	(km)	
63	10	13	5	17	57.1	44.8	149.5	60	8.1
64	7	24	8	12	40.0	47.2	153.8	33	7.0
68	1	29	10	19	5.6	43.6	146.7	40	7.0
69	8	11	21	27	39.4	43.5	147.4	28	7.8
71	12	15	8	29	55.3	56.0	163.3	33	7.8
73	6	17	3	55	2.9	43.2	145.8	48	7.7

Fig. 2. Magnitude-frequency relations of October 1963 and August 1969 sequences.

aftershocks that occurred during 30 days after the main shock and within 200 km distance from it were adopted in both of Fig. 2 (1) and (2). Gutenberg-Richter's law seems to hold good in a range of magnitude greater than 4.5 for both sequences. We must take care to use data of smaller aftershocks. For the statistical analysis in later sections, we shall use the data of shocks with magnitudes greater than 4.5.

3. Time-space analyses of aftershock sequences

Time-space plots (figures with time and space axes) are often useful to see time variation of seismic active area. These plots sometimes give a good idea for investigations on seismic activity. However, space distribution of earthquakes in three dimensions is usually projected onto a line, and difference of direction of the line sometimes makes a quite different impression. What direction should be selected to obtain the best feature for representing physical meanings? We shall investigate the time variations of aftershock areas by the following statistical method and show how we can find the best direction of the projection line.

3.1 Method

Seismic activity is represented by the five parameters, origin time, hypocenter coordinates, and magnitude. Among these five parameters, time-space interaction is

important to see time variation of an aftershock area. If earthquakes in one sequence show propagative activity exactly in one direction, the apparent velocity between every two earthquakes

$$v_{ij} = \Delta x_{ij} / \Delta t_{ij}$$

where

Δx_{ij}: distance interval between **event** i and j

Δt_{ij}: time interval between **event** i and j,

will be equal to the speed of propagation. The $\Delta x_{ij} - \Delta t_{ij}$ relationship may give a hint for aftershock migrations.

Kagan and Knopoff[9] investigated a time-space-magnitude relationship among worldwide earthquakes of magnitudes greater than 7 by a statistical method. They assumed that earthquakes have a Poissonian distribution and compared the actual rate of occurrence of subsequent shocks in any time interval with the value calculated from the Poissonian. They examined the propability of occurrence of earthquakes actually obtained in each time-distance interval. According to them, some of these time-distance intervals in which earthquakes occurred much more frequently than expected by the Poissonian rate are explainable by the time-space relationship of a migration.

We do not assume any stochastic process such as Poisson process in their case to be compared with any actual process, but it is assumed that spatial distribution is independent of time. We examined how much inconsistency will occur on this assumption. The propability density of aftershock occurrence, $\rho(\boldsymbol{x}, t)$, is assumed to be the following,

$$\rho(\boldsymbol{x}, t) = \rho_1(\boldsymbol{x}) \cdot \rho_2(t) \qquad (1)$$

Integrating this function with respect to time in a certain period, a spacial distribution is obtained. In the same way, integrating with respect to space within a certain volume, a time-frequency relation is obtained. Distributions of pairs in relation to a certain time-distance interval, $\varphi(\Delta x, \Delta t)$, are derived from $\rho(\boldsymbol{x}, t)$, as follows;

$$\varphi(\Delta x, \Delta t) = \iint_{V T} \rho(\boldsymbol{s}, u) \cdot \rho(\boldsymbol{s} + \Delta x, u + \Delta t) \, du \, d\boldsymbol{s}. \qquad (2)$$

Substituting Eq. (1) into Eq. (2), we have

$$\varphi(\Delta x, \Delta t) = \iint_{V T} \rho_1(\boldsymbol{s}) \cdot \rho_1(\boldsymbol{s} + \Delta x) \cdot \rho_2(u) \cdot \rho_2(u + \Delta t) \, du \, d\boldsymbol{s}$$

$$= \int_V \rho_1(\boldsymbol{s}) \cdot \rho_1(\boldsymbol{s} + \Delta x) \, d\boldsymbol{s} \int_T \rho_2(u) \cdot \rho_2(u + \Delta t) \, du. \qquad (3)$$

Assuming that a domain V is so large that

$$\rho_1(\boldsymbol{s}) = 0$$

outside V,

$$\varphi(\varDelta x,\ \varDelta t) = \psi(-\varDelta x,\ \varDelta t) \qquad\qquad (4)$$

is derived from Eq. (3). This equation means that a distribution of pairs in relation to $\varDelta x$ is expected to be symmetric with respect to the origin in any time interval $\varDelta t$. In practice, integrals are replaced by summations. Aftershocks adopted in later analysis will be restricted to a certain domain V, so that the above assumption, $\rho_1(s) = 0$ outside V, shall be accepted.

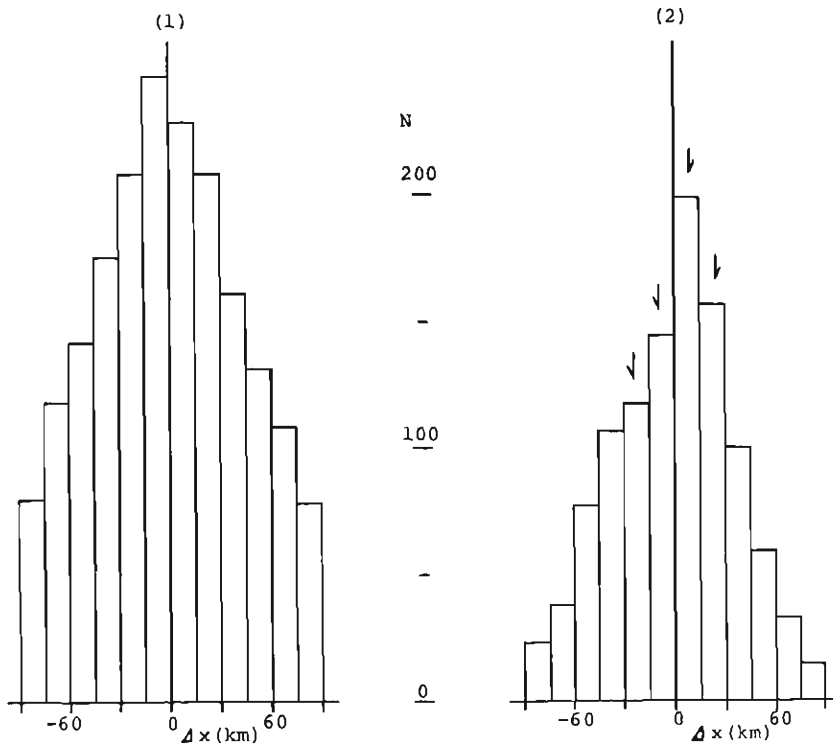Examples of symmetric and disturbed cases are seen in Fig. 3 (1) and (2).

Fig. 3. Histograms of pairs in a certain time interval. (1) An example of symmetric case, (2) an example of disturbed case. Arrows indicate distance intervals of disturbance.

These are the histograms of pairs at every 15 km intervals and a certain range of time intervals $(\varDelta t - \delta \sim \varDelta t + \delta)$. In Fig. 3 (2) (a disturbed case), symmetry is disturbed near $\varDelta x = 15$ km or -15 km (indicated by arrows), that is, pairs in the distance intervals of $\varDelta x = 0 \sim 15$ and $15 \sim 30$ km are more frequent than those in the corresponding intervals of $\varDelta x = 0 \sim -15$ and $-15 \sim -30$ km. We may suspect that this excess of pairs in $\varDelta x = 0 \sim 30$ km is caused by propagation of activity and that the velocity of propagation will be nearly equal to the apparent velocity, $\varDelta x / \varDelta t$.

3.2 Aftershock sequence of August 1969

The hypocentral parameters of the main shock are given in Table 1. Fault parameters were calculated by Abe.[10] The fault-plane solution is shown in Fig. 4. Abe concluded that the actual dislocation took place over a gently dipping
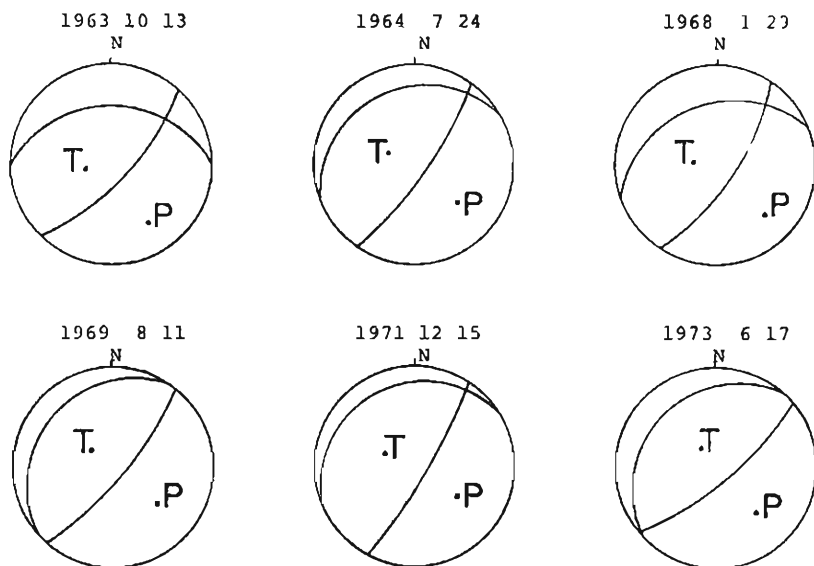

Fig. 4. Fault-plane solutions of the main shocks. [10],[23]

nodal plane, considering a large aftershock area and slip directions of neighboring earthquakes. Hatori[11] estimated source area of tsunami generated by this shock. This agreed with the aftershock area. One of the present authors[12] reported that just before the main shock, a few large foreshocks occurred and migrated to landward side of the aftershock area where the main shock took place. Motoya[13] investigated the aftershock activity with the data observed by sensitive seismographs at Urakawa and reported that the decay of frequency of aftershocks with time is well represented by an equation $n(t) = A \cdot (t+c)^{-p}$ ($p=1.0$, $c=0.02$ days). Santo[8] pointed out the migration of this sequence. We have investigated the aftershock activity of this sequence in more detail by the method mentioned above.

Fig. 5-(4) shows the epicenter distribution of the aftershocks during 20000 minutes (about 2 weeks) after the main shock. From these aftershocks, we selected about 120 shocks which occurred within 100 km distance from the main shock in both directions normal and parallel to the trench axis, and whose magnitudes are greater than 4.5. The range of magnitudes greater than 4.5 seems to be relatively narrow, so that it does not seem necessary to take magnitude as a parameter. The focal depth is generally less accurate than horizontal coordinates, and also the change of
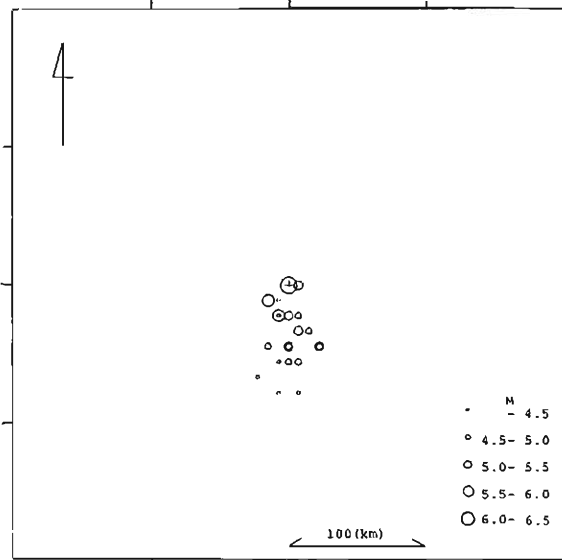
1963 10   13 44.8   149.5

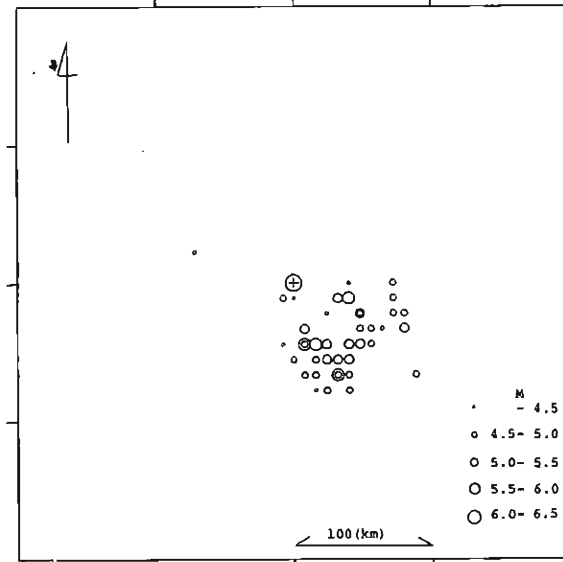0   —   20000
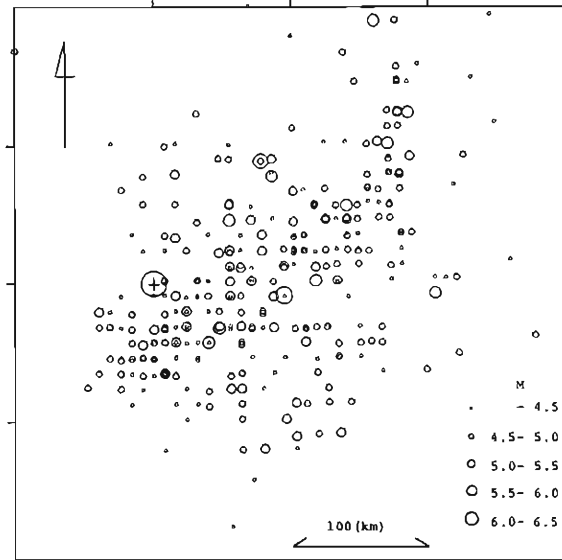
(1)

1964 7   24 46.9   153.9
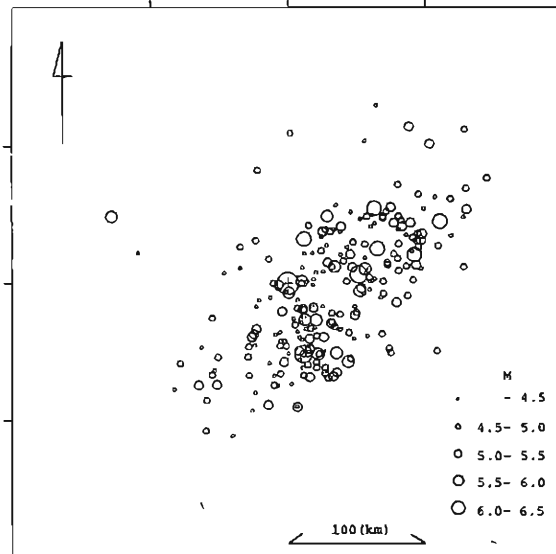
0   —   20000

(2)

1968 1   29 43.6   146.7

0   —   20000

(3)

1969 8   11 43.5   147.4

0   —   20000

(4)

1971 12 15 56.0 163.3

0 — 20000

(5)

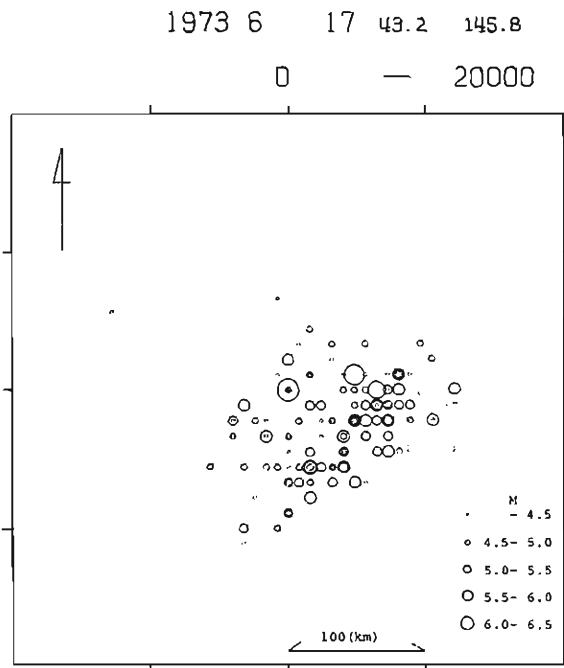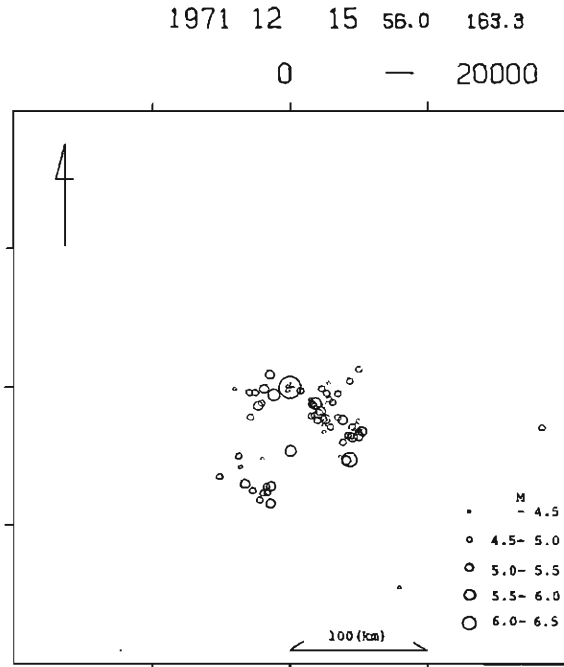1973 6 17 43.2 145.8

0 — 20000

(6)

Fig. 5. Epicenters of aftershocks during 20000 minutes after the main shocks. The largest circle at a cross mark indicates the main shock.
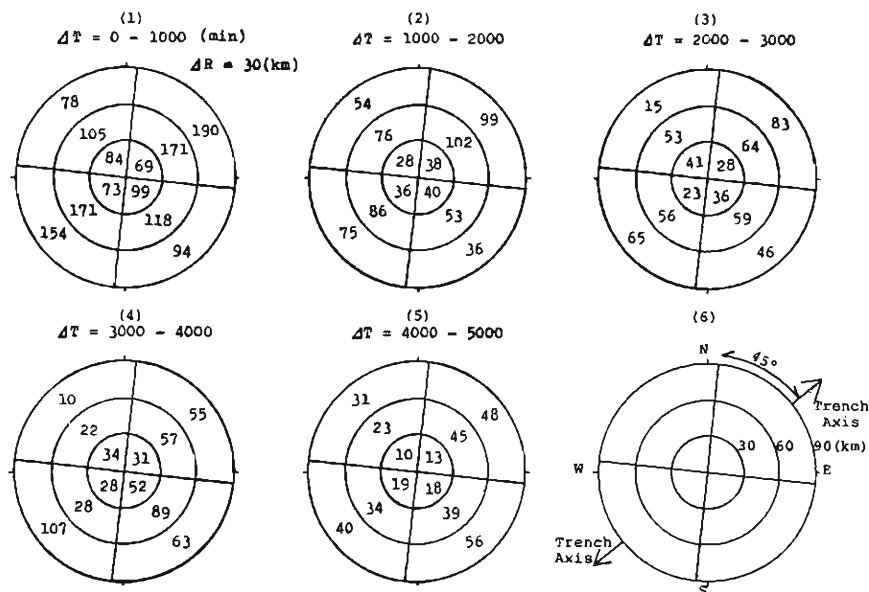
Fig. 6. Numbers of pairs in each time-space interval of August 1969 sequence.
Coordinate system is referred to the trench axis as Fig. 6-(6).

focal depths seems to be rather small on the gently dipping fault plane. Therefore we use only three parameters of origin time and horizontal coordinates among the five parameters. The distributions of Δx are shown at successive 1000 minutes intervals in Fig. 6. As seen, Δx are represented by a polar coordinate system. The azimuth is classified into four quadrants, referring to the trench axis. Two rows of numerals from upper-right to lower-left and from upper-left to lower-right represent numbers of pairs parallel and normal to the trench axis, respectively. Fig. 6-(1) seems to show something symmetric with respect to the origin. On the other hand, in Fig. 6-(4), the distance intervals of 30~60 and 60~90 km have 22 and 10 pairs of NW direction and 89 and 63 pairs of SE direction, respectively. This figure does not show symmetry at all. This suggests that aftershock activity is apt to propagate in the SE direction (seaward). The ratio of NW—SE direction to total tends to increase with time, that is 41. 1, 39. 7, 44. 0, 46. 9, and 47. 1(%). This means that shocks during short time intervals after any shock are apt to occur in NE—SW direction, and that with increase of time interval, activity of NW—SE direction, particularly SE direction becomes high.

Next, we estimate the speed and direction of migration. We used three parameters of (Δx, Δt) above. Hereafter we use only two parameters of (Δx, Δt) by projecting vector Δx on one line. An example is seen in Table 2. The line of projection is oriented in S40°E (positive) —N40°W (negative) direction. In every time-distance interval each entry is a ratio of the number of pairs in positive

Table 2. An example of time-space analysis of August 1969 sequence. Abscissa is time interval from one shock to another later shock, and ordinate is distance interval from the former of the pair to the later along S40°E (positive)-N40°W (negative) direction. Each entry indicates the ratio of number of pairs in positive direction to the total of both directions. Numbers with brackets are the total values. In the case that a hypothesis, a ratio is equal to 0.5, is rejected, the entry is underlined.

Distance interval (km)	0–1000	1000–2000	2000–3000	3000–4000	4000–5000
75–90	0.54 (56)	0.37 (35)	0.52 (21)	<u>0.96</u> (27)	0.70 (27)
60–75	0.52 (113)	0.47 (70)	<u>0.65</u> (54)	<u>0.84</u> (64)	0.71 (59)
45–60	0.57 (238)	0.46 (125)	0.65 (97)	0.85 (108)	0.64 (91)
30–45	0.50 (371)	0.48 (206)	0.57 (188)	0.83 (161)	0.69 (99)
15–30	0.56 (552)	0.57 (273)	0.54 (260)	0.70 (209)	0.58 (113)
0–15	0.54 (662)	0.57 (334)	0.55 (260)	0.49 (234)	0.56 (126)

Time interval (min)

$$\frac{S40°E}{S40°E+N40°W}, \quad (S40°E+N40°W)$$

direction to total of both directions (the same distance interval but opposite direction). The total number is also shown with brackets in each interval. This ratio is an indicator of the symmetry, and is expected to be 0.5 in a symmetric case. With some exceptions, the ratio is larger than 0.5 in Table 2. Under a null hypothesis that both directions have the same propability (0.5), the binominal test is used at the level of significance of 5%. The entry is underlined in the case that this hypothesis is rejected. As we examine these underlined entries, it seems that the asymmetric case takes place in farther distance interval with increase of time interval. This might show the seaward propagation of aftershock activity. We estimate the speed at 10~35 km/day.

Fig. 7 shows the results concerned with other directions of projection lines. The direction of the line is set for every 30 degrees from parallel to the trench axis. The six lines in the figure show these directions. They intersect at the epicenter of the main shock. The longer part of each line shows the positive direction in projection. Six inserted figures are obtained in the same way as Table 2, ordinate
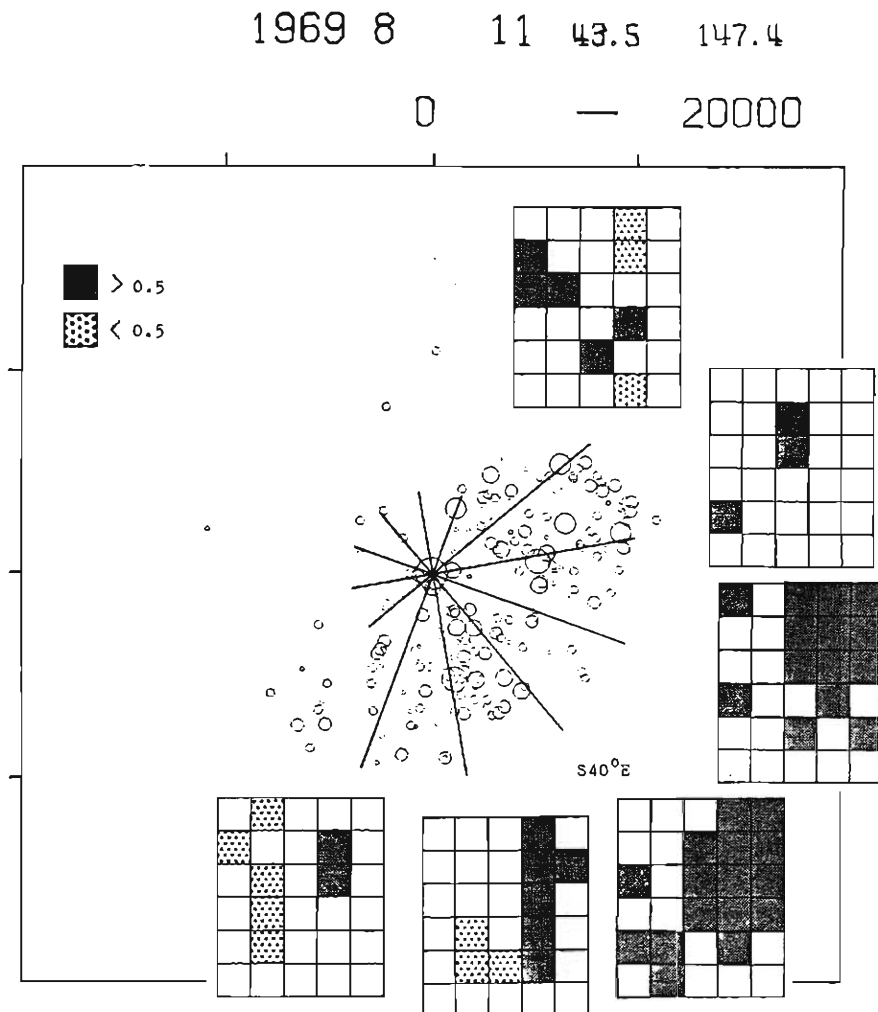
Fig. 7. Results of time-space analysis of August 1969. Six lines indicate directions of projection. Inserted figures are results of analysis in respective directions of projection. Ordinate and abscissa are graduated in every 15 km of distance interval and 1000 minutes of time interval, respectively. A black block shows that a ratio of the number of pairs in positive direction to the total of both directions is expected to be greater than 0.5 by a binominal test. A dotted block shows that a ratio is to be smaller than 0.5. A blank block shows the other case. Epicenters of aftershocks are also shown (see Fig. 5-(4)).

and abscissa are graduated in every 15 km of distance interval and 1000 minute of time interval, respectively. The binominal test was used in each time-distance interval, and the result is represented in three ways as follows: A blank means that null hypothesis is not rejected. The black means that the hypothesis is rejected and that

the propability of positive direction is expected to be larger than 0.5. The dotted means that the hypothesis is also rejected and that the propability is to be smaller than 0.5. As seen in Fig. 7, the symmetry is largely disturbed in the cases of S70°E and S40°E directions. If we assume that the migration is one directional, or unilateral, the direction is most likely to be normal to the trench axis or somewhat counterclockwise. The speed is estimated at 10–35 km/day as before.

3.3 Aftershock sequence of June 1973

This earthquake occurred on June 17, 1973 in eastern Hokkaido. It had been predicted on the basis of a seismicity gap.[14] The faulting nature of this earthquake is considered to be similar to those of neighboring great earthquakes (see Fig. 4),
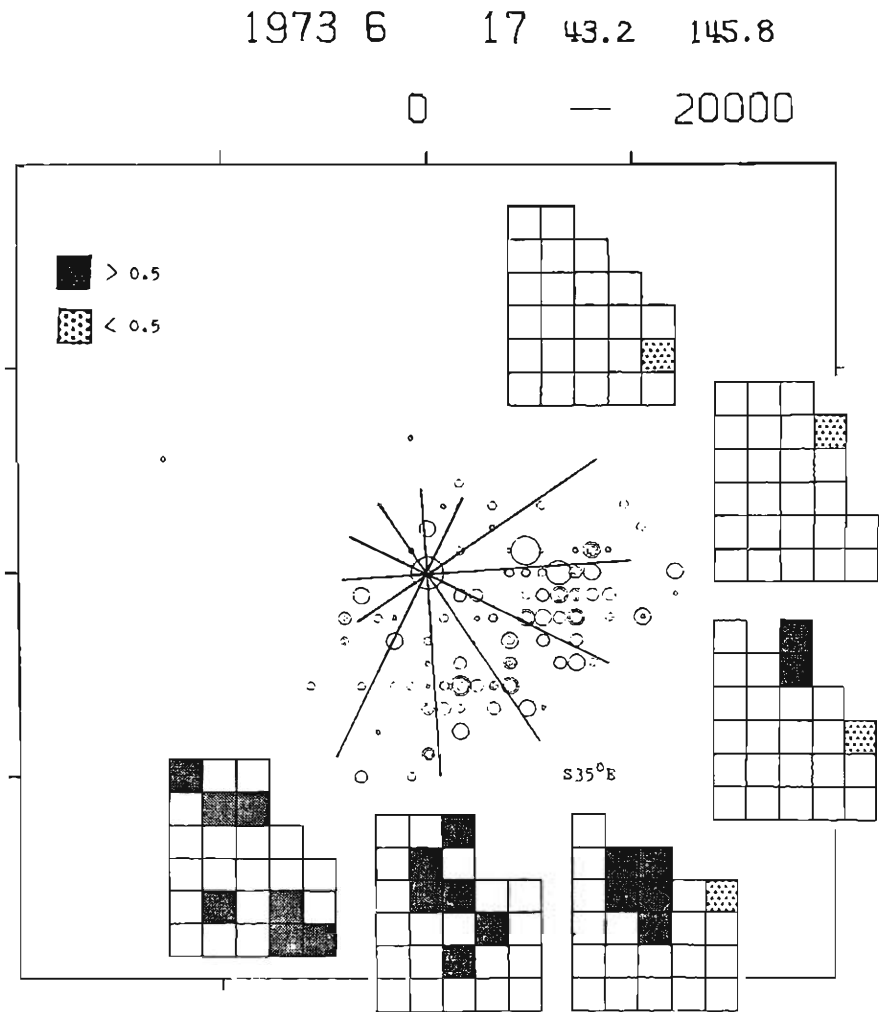

Fig. 8. Results of time-space analysis of June 1973. Notations are the same as those of Fig. 7.

but in quantity this shock was smaller by a factor of 3~5[15],[16] than the earthquake
in the previous section. The epicenters of aftershocks are plotted in Fig. 5-(6).
Number of aftershocks is smaller than that of the previous case. In the same way
as the previous, we investigate migration of this sequence. The results are shown
in Fig. 8 with the same notations as those in Fig. 7. The upper-right parts of
inserted figures are cut off because of scanty data. It seems that the symmetry is
most largely disturbed in the direction normal to the trench axis. It might be
concluded that the direction of propagation, on the assumption of unilateral propagation,
is seaward. The speed of the propagation is estimated at 20−50 km/day.

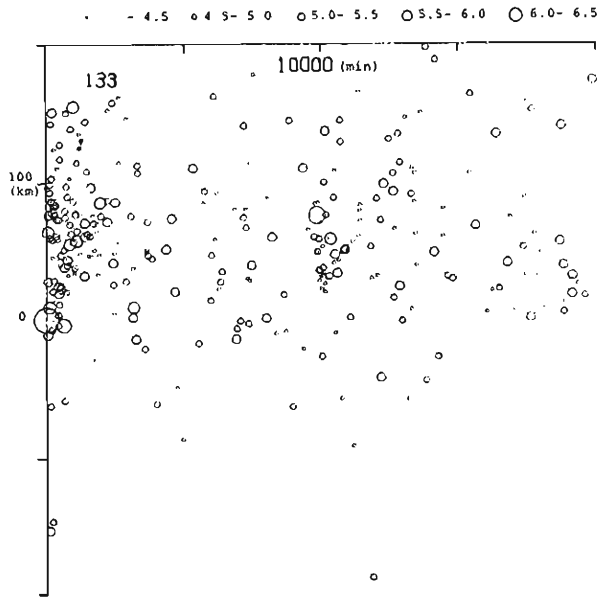### 3.4 Time-space plots of sequences

In Kuril, many large earthquakes occurred recently. Among them, the shocks
followed by many aftershocks are listed in Table 1. These have been already
investigated by many authors.[17]−[23] These main shocks are situated on landward side
of their aftershock areas (see Fig. 5). The fault-plane solutions are given in Fig. 4.
These shocks seem to be of the similar faulting nature, for example, a low angle
thrust fault.

Fig. 9 shows time-space plots of those sequences, where epicenters of shocks
are projected on a line normal to the trench axis. Ordinate and abscissa indicate
the distance from, and the time lapse after the main shock, respectively. Each of
Fig. 9 (1)-(6) shows a migration feature well. Particularly in Fig. 9 (2), (3) and
(5), a quiescent area of activity originates at the epicenter of the main shock, and
spreads seaward with time. Such a feature appears in the other cases, although it
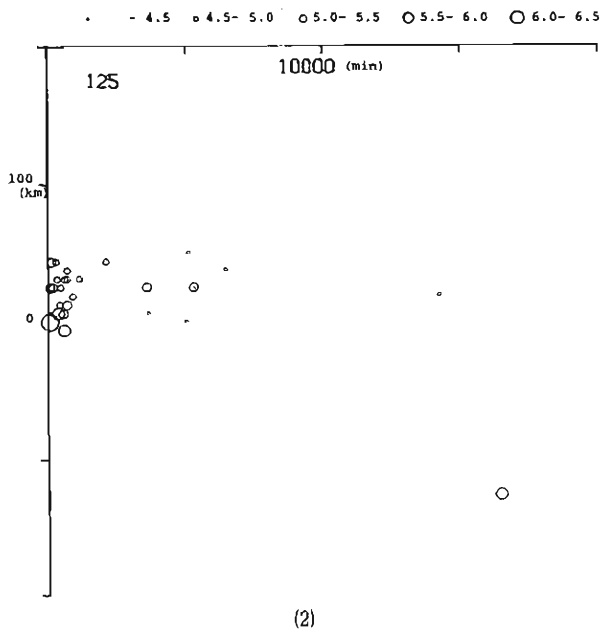is not so clear. Spreading speeds are 8−16 km/day.

4. Discussion and conclusion

One of the present authors[24] has already reported such a migration feature of
aftershock activities in other regions as those mentioned in the previous sections.
A spreading speed of quiescent area is summarized in Table 3. These values were
estimated visually from time-space plots such as Fig. 9. In each case of August
1969 and June 1973, the speed in Table 3 is lower than that estimated previously
by the statistical method. Because the former represented a propagation velocity of
relatively high seismicity, and the latter represented the velocity of lower limit. The
difference between two values estimated by different methods is at most a fatcor 2~4.
It may be concluded that the propagation speed of aftershock sequences in Kuril is
the same order as that of San Fernand earthquake,[1] and on the other hand much
lower than those of Alaska and Aleutian sequences.[6] In Kuril, the fault width of a
large thrust earthquake is about 100 km, and propagation speed is about 10 km/day.
Then, the migration should be observed during only about 10 days just after a main
shock. Even if migrations are concerned in a crustal movement, it is difficult to
detect this short time deformation by leveling. Tada[22] reported crustal movement
during a short period after the 1973 Nemuro-Oki Earthquake on the basis of tide
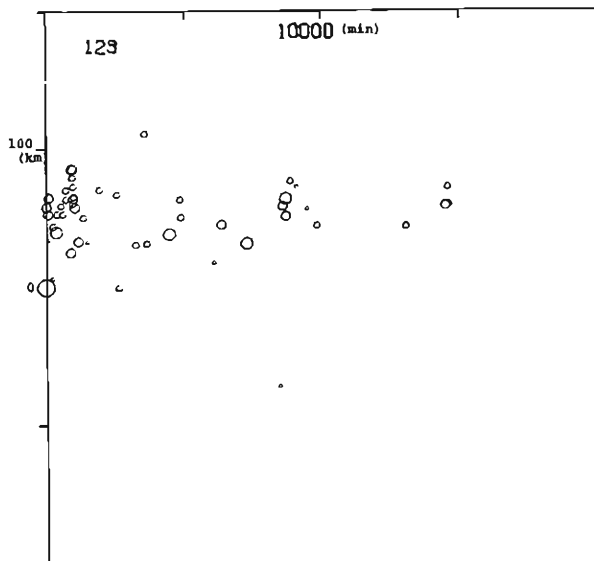
1963 10 13 44.8 149.5

- 4.5 o 4 5- 5 0 o 5.0- 5.5 ○ 5.5- 6.0 ◯ 6.0- 6.5
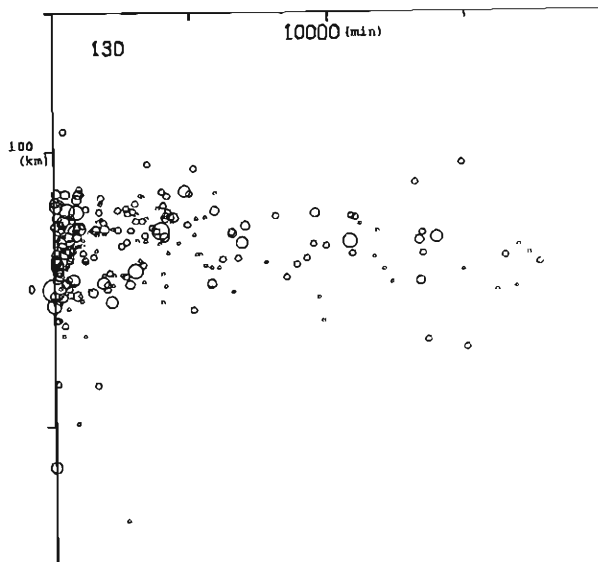
10000 (min)

133

100 (km)

0

(1)

1964 7 24 46.9 153.9

- 4.5 o 4.5- 5.0 o 5.0- 5.5 ○ 5.5- 6.0 ◯ 6.0- 6.5

10000 (min)

125

100 (km)

0

(2)

1968 1   29 43.6   146.7

(3)

1969 8   11 43.5   147.4

(4)

1971 12   15 56.0   163.3
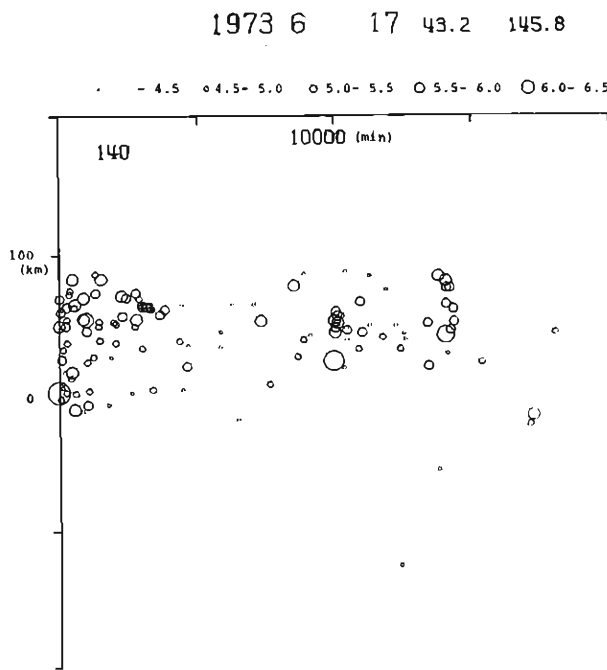

(5)

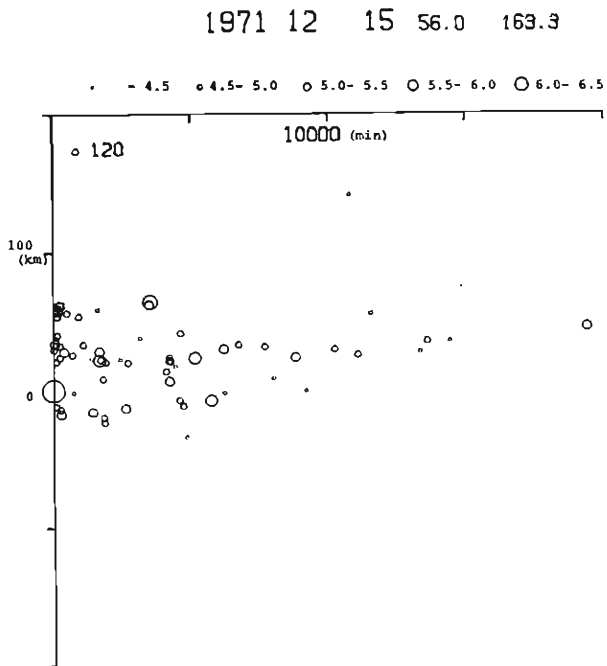## 1973 6   17 43.2   145.8

(6)

Fig. 9. Time-space plots of sequences. Ordinate and abscissa indicate the distance from and the time lapse after the main shock, respectively. The number at a upper-left corner is the azimuth of a projection line counted clockwise from the north.

Table 3. Spreading velocities of quiescent areas.

Date Y	M	D	Epicenter Lat.	Lon.	Velocity (km/day)
1970	4	29	14.5°N	92.6°W	11
1971	7	9	32.5°S	71.2°W	15
1972	12	2	6.5°N	126.6°E	7
1964	7	24	47.3°N	153.8°E	8
1968	1	29	43.6°N	146.7°E	8
1969	8	11	43.5°N	147.4°E	9
1971	12	15	56.0°N	163.3°E	9
1973	6	17	43.2°N	145.8°E	13

gauge records.

In any case, detailed researches for mechanisms of migrations are left for future study. Our conclusions summarized as follows:

1) On the assumption of unilateral propagation, the direction of propagation is likely to be normal to the trench axis.

2) Time-space plots, where epicenters of aftershocks are projected onto the line normal to the trench axis, show that the quiescent area starts at the epicenter of the main shock and spreads seaward.

3) Propagation speeds of aftershock sequences are estimated at 8~50 km/day.

Acknowledgement

References

1) Whitcomb, J. H., C. R. Allen, J. D. Garmany and J. A. Hileman: San Fernando Earthquake Series, 1971: Focal Mechanisms and Tectonics, Rev. Geophys. Space Phys., Vol. 11, 1973, pp. 693-730.

2) Yamakawa, N.: Aftershocks and Focal Mechanisms of Main shocks, Geophys. Mag., Vol. 36, 1972, pp. 15-30.

3) Kanamori, H.: Synthesis of Long-Period Surface Waves and Its Application to Earthquake Source Studies-Kurile Islands Earthquake of October 13, 1963-, J. Geophys. Res., Vol. 75 No. 26, 1970, pp. 5011-5027.

4) Kelleher, J., L. Sykes and J. Oliver: Possible Criteria for Predicting Earthquake Locations and Their Application to Major Plate Boundaries of the Pacific and the Caribbean, J. Geophys. Res., Vol. 78 No. 14, 1973, pp. 2547-2585.

5) Imoto, M. and Y. Kishimoto: On a Bias of Aftershock Epicenters at Trenches of the

Pacific Ocean, Disas. Prev. Res. Inst. Kyoto Univ. Annuals, No. 20, 1977, (in Japanese, in preparation).

6) Mogi, K.: Development of Aftershock Areas of Great Earthquakes, Bull. Earthquake Res. Inst. Tokyo Univ., Vol. 46, 1968, pp. 175-203.

7) Ida, Y.: Slow-Moving Deformation Pulses along Tectonic Faults, Phys. Earth Panet. Inter., Vol. 9, 1974, pp. 328-337.

8) Santo, T.: Regional Study on the Characteristic Seismicity of the World. Part VII. -Activity of Aftershocks in Kuril Islands Region-, Bull. Intern. Inst. Earthq. Engin., Vol. 7, 1970, pp. 119-131.

9) Kagan, Y. and L. Knopoff: Statistical Search for Non-Random Features of the Seismicity of Strong Earthquake, Phys. Earth Planet. Inter., Vol. 12, 1976, pp. 291-318.

10) Abe, K.: Tsunami and Mechanism of Great Earthquake, Phys. Earth Planet. Inter., Vol. 7, 1973, pp. 143-153.

11) Hatori, T.: An Investigation of the Tsunami generated by the East Hokkaido Earthquake of August, 1969., Bull. Earthquake Res. Inst. Tokyo Univ., Vol. 48, 1970, pp. 399-412.

12) Imoto, M.: On a Starting Point of the Large Fracture of August 11, 1969 Hokkaido Toho-oki Earthquake, Zisin, Ser. II Vol. 29 No. 1, 1976, pp. 1-13 (in Japanese).

13) Motoya, Y.: Aftershock Sequence of the Earthquake East off Hokkaido on August 12, 1969, Geophys. Bull. Hokkaido Univ., Vol. 24, 1970, pp. 93-106 (in Japanese).

14) Utsu, T.: Large Earthquake near Hokkaido and the Expectancy of the Occurrence of a Large Earthquake off Nemuro, Rep. Coord. Comm. Earthquake Pre. Geogr. Surv. Inst., Vol. 7, 1972, pp. 7-13 (in Japanese).

15) Shimazaki, K.: Nemuro-Oki Earthquake of June 17, 1973: A Lithosheric Rebound at the Upper Half of the Inteface, Phys. Earth Planet. Inter., Vol. 9, 1974, pp. 314-327.

16) Hatori, T.: Tsunami Activity in Eastern Hokkaido after the Nemuro Peninsula Earthquake in 1973, Zisin, Ser. II Vol. 28 No. 4, 1975, pp. 461-471.

17) Santo, T.: Shock Sequence of the Southern Kurile Islands from October 09 to December 31, 1963, Bull. Intern. Inst. Seism. Earthq. Engin., Vol. 1, 1964, pp. 33-54.

18) Yamakawa, N., M. Kishio and K. Abe: Spacial and Time Distributions of Foreshocks and Aftershocks of the Earthquke near the Southern Kuril Islands on 13 October 1963, Geophy. Mag., Vol. 34 No. 3, 1969, pp. 277-306.

19) Maki, T.: Focal Mechanisms of the 1963 Itrup Earthquake Sequence, Geophys. Bull. Hokkaido Univ., Vol. 19, 1968, pp. 21-55 (in Japanese).

20) Hirota, T.: Aftershock Sequence of the Earthquake off Shikotan Island on January 29, 1968, Geophys. Bull. Hokkaido Univ., Vol. 21, 1968, pp. 93-106 (in Japanese).

21) Tada, T.: Fault Model and Crustal Movement of the 1973 Nemuro-Oki Earthquake, Zisin, Ser. II Vol. 27 No. 2, 1974, pp. 120-128 (in Japanese).

22) Tada, T.: Anelastic Recovering Fault Motion of Continental Plate Immediately after the 1973 Nemuro-Oki Earthquake, Zisin, Ser. 2 Vol. 27 No. 2, 1974, pp. 167-169 (in Japanese).

23) Stauder, W. and L. Mualchin: Fault Motion in the Large Earthquakes of the Kuril-Kamchatka Arc and of the Kuril-Hokkaido Corner, J. Geophys. Res., Vol. 81 No. 2, 1976, pp. 297-308.

24) Imoto, M.: Presented at the Spring Meeting Seism. Soc. Japan (14 May 1977).

On the Measurement of V_p/V_s Ratio in the Area around Lake Biwa

By Fumiaki TAKEUCHI, Kazuo MINO, and Masajiro IMOTO

(Manuscript received October 5, 1977)

Abstract

It has been reported that the vertical movement of the crust at the west coast of Lake Biwa changed its mode recently.[1]

The large active fault, Hanaore is very near the region. Encouraged by these facts, many researchers have carried out gravity measurements, measuring of vertical and horizontal movements of the crust, observation of micro-earthquakes in and around the region, and other geophysical studies. The authors are among them and they calculated V_p/V_s ratio using the data at the net stations of Hokuriku Micro-earthquake Observatory, Abuyama Seismological Observatory and at some temporal stations. The averaged value of V_p/V_s has been determined to be 1.673. Smaller values than this are of the stations near the coast.

Special stations were set for about a month along the Hanaore fault to catch the seismic waves from the Wakayama region, and two earthquakes occurred during the time. The V_p/V_s ratio of the two earthquakes were in the interval 1.70 to 1.75 for almost all the stations.

1. Introduction

V_p/V_s ratio indicates the nature of the media in which the seismic waves run through, and the low value of it in the crust may be a sign of earthquake occurrence. Many investigators have studied on the value in various regions, especially on its time variance. And many of their studies are listed by Ohtake and Katsumata[2] as reference papers. Some of the works state that the ratio seemed to decrease before an earthquake event, and some of the others state otherwise.

Here the authors calculate the V_p/V_s values at the region around Lake Biwa, which will be an elementary factor to discuss whether a large earthquake will occur near the region in the future or not.

2. V_p/V_s calculated by the formula $1 + (T_{sp}/T_p)$

Seismicity maps and some characteristic features of them have been already reported and discussed.[3]

Fig. 1 represents the distribution of epicenters, which were relocated for the use of V_p/V_s calculation. More than four p times were used to determine a hypocenter location and the origin time by means of the least square method. 885 was the number of earthquakes thus located whose depths were less than 50 km and the mean residual remained smaller than or equal to 0.2 sec. from Aug. 1975 to Jul. 1976. Fig. 2a shows the p wave velocity structure of the crust on which the travel
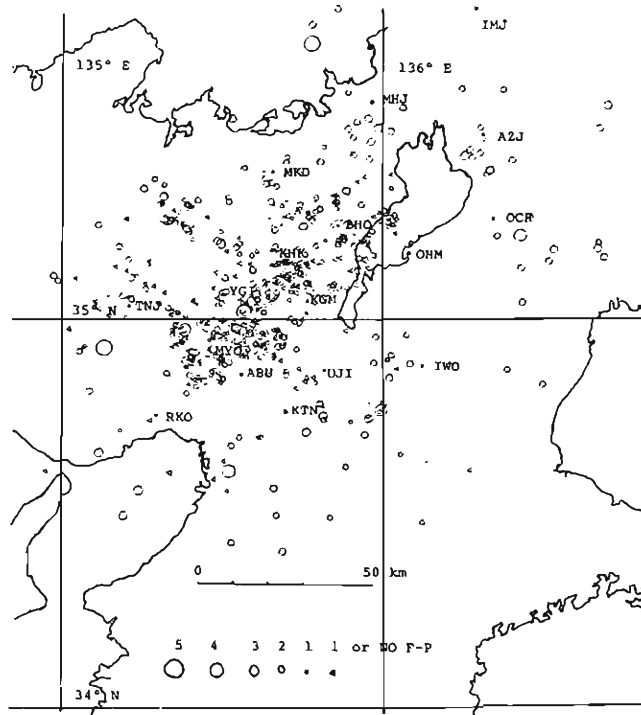
Fig. 1. Distribution of 885 eipcenters relocated for the present paper. These are
selected from the data obtained at 17 stations in the figure, from August
1975 to July 1976 by the conditions that the depth is less than 50 km and
the mean residual of p times is less than or equal to 0.2 sec. Radii of the
circles indicate magnitudes of the earthquakes as the examples at the bottom
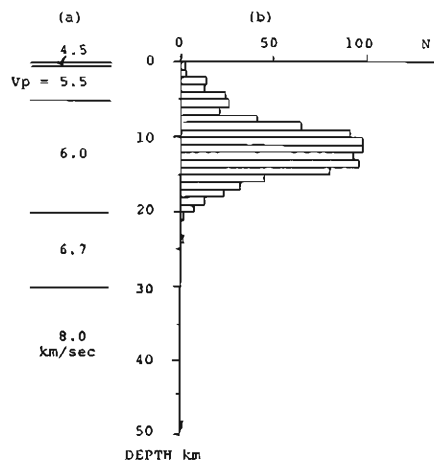of the map.

Fig. 2. (a) Structure of p wave velocity assumed to calculate travel times.
        (b) Frequency distribution of focal depths of the same earthquakes
             plotted in Fig. 1.

Table 1. Mean value of Vp/Vs ratio at each station. In the second column
       are the numbers of available data.

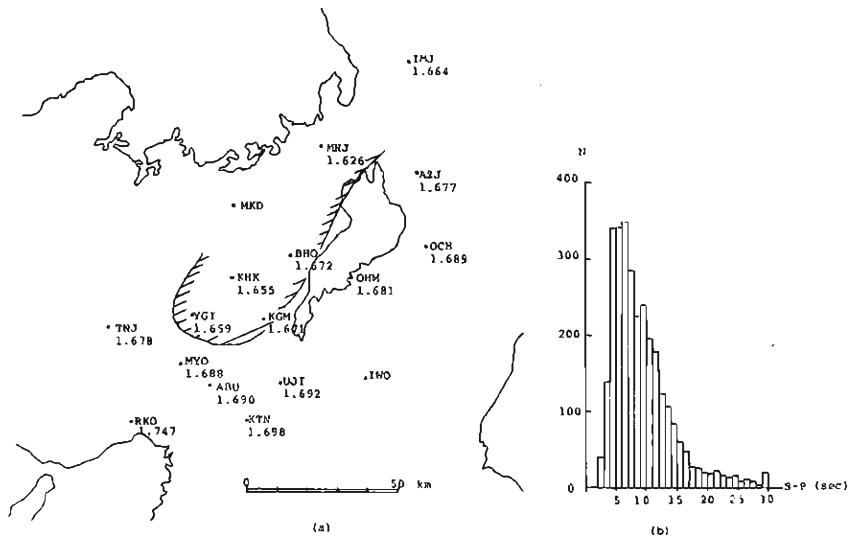| STATION	NUMBER	Vp/Vs RATIO
MHJ	14	1. 626±0. 085
KHK	368	1. 655±0. 051
YGI	481	1. 659 ±0. 044
IMJ	3	1. 664±0. 018
KGM	423	1. 671±0. 045
BHO	269	1. 672±0. 061
AZJ	27	1. 677±0. 081
TNJ	402	1. 678±0. 058
OHM	203	1. 681±0. 055
MYO	231	1. 688±0. 060
OCH	21	1. 689±0. 045
ABU	262	1. 690±0. 058
UJI	164	1. 692±0. 067
KTN	94	1. 698±0. 071
RKO	31	1. 747±0. 071
TOTAL	2993	1. 673±0. 081

Fig. 3. (a) Mean value of Vp/Vs ratio at each station. Region of lower Vp/Vs
           than the mean value (1. 673) is hatched.
       (b) Frequency distribution of S-Ptimes.

times were calculated. Fig. 2b is the frequency distribution of focal depths. V_p/V_s value was calculated by the formula $1+(T_{sp}/T_p)$, where T_{sp} and T_p are the $S-P$ and the $P-O$ times respectively. P and $S-P$ times of c, d ranks, that is, reading errors greater than 0.2 sec, were omitted from the data, and thus the number of available sets of data came down to 2993. Fig. 3a shows the mean value of V_p/V_s over all data at each station. The values are also listed on Table 1. with their standard deviations. The deviations seem to be very large, but the number of data is also large, so the confidence intervals with 95% significance are far narrower for most stations. The mean of total data, 1.673, is rather small compared with that of Hashizume's result.[4] In fig. 3a., the region of lower V_p/V_s than the mean value is hatched. Frequency distributions of $S-P$ times (Fig. 3b) and focal depths (Fig. 2b) show that the values above mentioned are largely depended on data of near and shallow earthquakes, so they may reflect the character of shallower part of the crust.

3. P time residuals

Mean values of p time residuals of the 885 earthquakes were obtained for the stations. (Fig. 4 and Table 2) The numbers in Fig. 4 and Table 2 are $O-C$ values, so the positive value indicates that the first motion of p waves was detected at the station later than the calculated time, which was based on the assumed p structure as in Fig. 2a. In Fig. 4 the positive areas of p residuals are hatched. Thick lines indicate the regions where the existance of a lower velocity layer (V_p=5.55 km/sec)
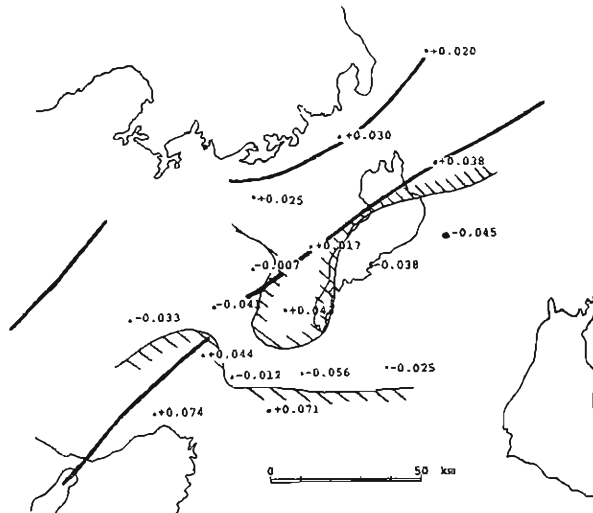

Fig. 4. Mean values of p time residuals. Hatched areas are those of the positive numbers which denote that the actual p wave velocity is lower than the calculated value. These areas show fairly good coincidence with the thick line region, where a low velocity layer was concluded to exist at the top of the crust by the Miboro Explosion.[5]

Table 2. Mean value of p time residuals at each station. Numbers of used data are in the second column.

STATION	NUMBER	P-TIME RESIDUAL
UJI	524	-0.056 ± 0.088
OCH	74	-0.045 ± 0.116
YGI	866	-0.041 ± 0.057
OHM	437	-0.038 ± 0.083
TNJ	790	-0.033 ± 0.071
IWO	150	-0.025 ± 0.117
ABU	553	-0.012 ± 0.092
KHK	732	-0.007 ± 0.058
BHO	553	0.017 ± 0.080
IMJ	7	0.020 ± 0.073
MKD	257	0.025 ± 0.105
MHJ	92	0.030 ± 0.087
AZJ	132	0.038 ± 0.119
KGM	780	0.043 ± 0.067
MYO	539	0.044 ± 0.088
KTN	275	0.071 ± 0.104
RKO	133	0.074 ± 0.102
TOTAL	6894	-0.002 ± 0.089

whose thickness is about 5 to 10 km at the top of the crust, just above the layer with V_p of 6 km/sec, was concluded by the Miboro Explosion.[5] These two regions show fairly good coincidence, and referring to Fig. 3a, it is concluded that the low velocity of p wave is one of the causes for low V_p/V_s ratio of the stations west of the lake. On the contrary, at MYO, KTN, and RKO stations, instead of low p wave velocity, V_p/V_s ratios are somewhat high.

4. Special observation of V_p/V_s

Five more stations were set during October 1975 along the Hanaore fault to catch seismic waves from Wakayama region, where earthquakes of magnitude larger

Table 3. Locations of the five special stations to catch earthquakes from Wakayama. These stations are on or very close to the Hanaore fault.

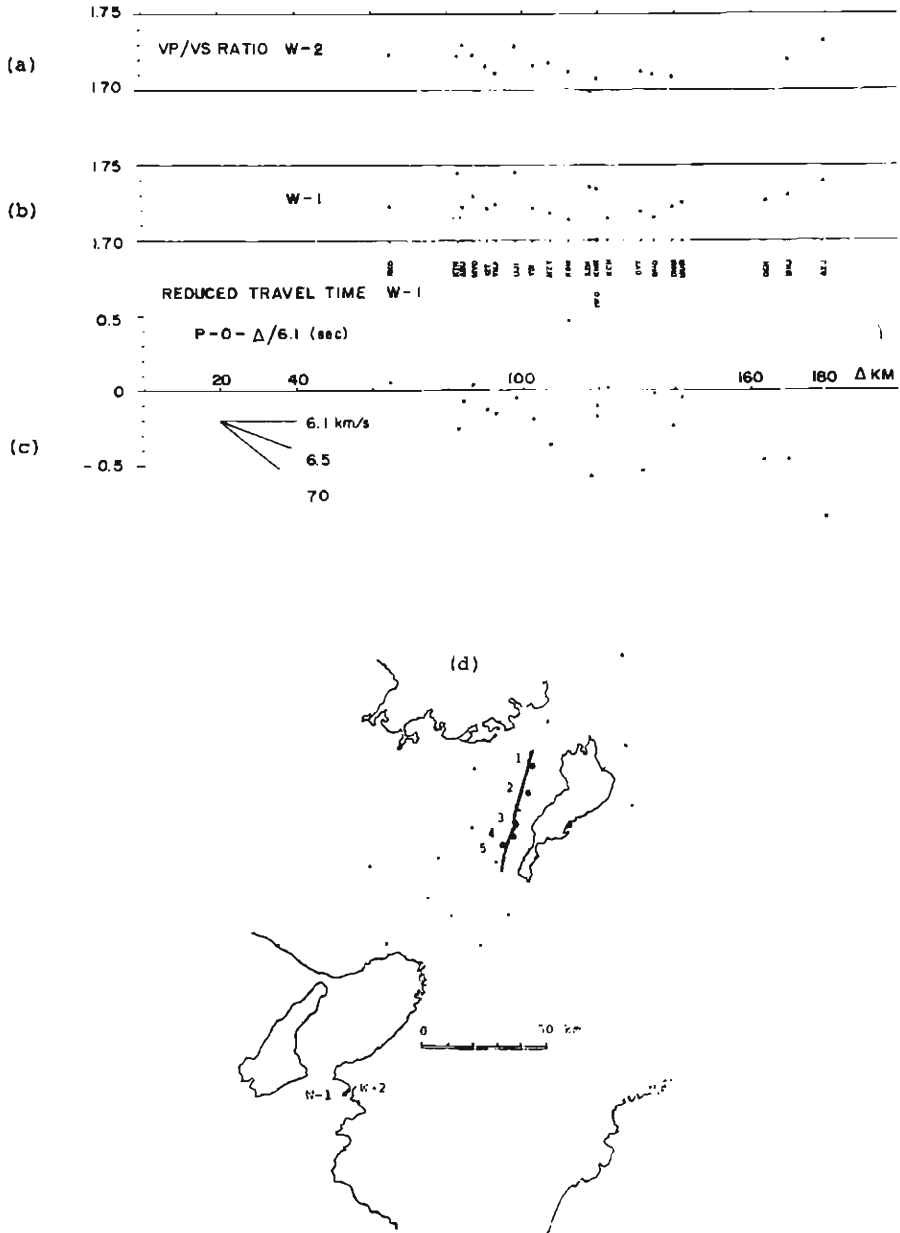| STATION	LATITUDE	LONGITUDE	MEMO	
SZH	35°06′15.60″ N	135°47′56.40″ E	Drums	1 Hz
KCH	35°08′07.00″ N	135°49′46.90″ E	FM rec.	1 Hz
TAI	35°11′38.00″ N	135°51′45.70″ E	DR rec.	4.5 Hz
MUR	35°18′36.60″ N	135°53′39.20″ E	DR rec	4.5 Hz
MKG	35°23′21.50″ N	135°55′19.50″ E	DR rec.	4.5 Hz

Fig. 5. (a) V_p/V_s ratio of W-2.
    (b) V_p/V_s ratio of W-1.
    (c) Reduced travel time of W-1. Apparent velocity at the stations farther than 123 km seems to be about 7 km/sec.
    (d) Locations of the five special stations. 1;MKG, 2;MUR, 3;TAI, 4; KCH, and 5;SZH. Small solid points are other routine stations. W-1 and W-2 are the epicenters. Solid line at the west coast of Lake Biwa is the Hanaore fault.

than 3 were expected often to occur. The locations of these stations are listed on Table 3. (Fig. 5d.) At three of these stations, MKG, MUR, and TAI, direct recording (DR) portable cassette recorders were used. Three or two components of pickups with natural frequency of 4.5 Hz and a crystal clock at each station were to ensure time accuracy of 0.02 sec for p and s first motions. At KCH station, an FM data recorder, pausing at normal times, was triggered to run when a large amplitude seismic wave came into the vertical component of the pickup. An analogue memory set worked all the time so as not to miss the first arrival. Three drum recorders were in use at SZH station. The natural frequency of six pickups at KCH and SZH stations were all 1 Hz.

On October 12, an earthquake (W-1), magnitude of which was 3.7, occurred in the region of Wakayama, which was followed by another earthquake (W-2, M=3.0) after one hour. Unfortunately the crystal timer at MKG had run down on the day and high amplitude of noise at TAI station covered the first arriving signal. P and s times obtained at the other three stations were served for analysis together with those at stations of routine observation. Calculation method is the same as was used in paragraph 2, but as the origin times, the values determined by Wakayama Micro –earthquake Observatory were adopted.[6] Fig. 5b shows the V_p/V_s values of W-1 earthquake and Fig. 5a W-2. Reduced travel time of W-1 is plotted for reference as Fig. 5c. Almost all the V_p/V_s values of both W-1 and W-2 fell between 1.70 and 1.75.

5. Discussion

The averaged V_p/V_s ratio calculated in paragraph 2 is about 1.673, and in paragraph 4 all values are larger than this by a few percents. One of the reasons to explain this disagreement is the difference of the methods of calculation in the two paragraphs, in other words, the difference of the determination methods of origin times. In fact, when we calculate V_p/V_s values by drawing a 'Wadati-diagram', which does not need the origin times, the averaged value of V_p/V_s's of the same earthquakes as are dealt with in the second paragraph is 1.69, a little greater than 1.673, while those of W-1 and W-2 calculated in this way still remain 1.73 and 1.72 respectively. Another possible reason is the difference of S-P times in the two cases. In paragraph 4, S-P times range from 7.68 sec to 21.10 sec, while in paragraph 2, most frequent S-P time is 6 or 7 sec as is shown in Fig. 3b. This suggests to us that the V_p/V_s value of W-1 and W-2 may largely reflect the nature of the deeper part of the crust or even the nature around the Moho discontinuity. Further more, the assumed structure of p wave velocity for them (Fig. 2a) is somewhat different from the actual one. If they are not so different from each other, the authors must have overlooked the first motion on the records at the stations whose epicentral distances of W-1 are farther than 123 km, at which distance Pn waves come as the first motion, and so the aparent velocity should be 8 km/sec, while as can be seen from Fig. 5c, it is measured as about 7 km/sec. But overlooking the wave does not

increase the V_p/V_s ratio, if the S phase is read in the right way.

6. Conclusions

V_p/V_s ratio is derived in two ways. For the first one it is 1. 673 as the averaged value, and the second, it is larger than 1. 70. This difference is partly explained by the difference of the wave paths in two cases. Lower values in the first method are of the stations at the west coast of Lake Biwa. This may result from the low velocity of p waves revealed in paragraph 3. These facts alone, however, are not enough to predict a large earthquake occurrence in the region in near future, for the V_p/V_s values obtained by the 'Wadati-diagram' method in paragraph 5 were not anomalously low.

It is desired to measure the seismic wave velocities again, when other evidences of earthquake precursors are found out in and around the region.

References

1) Danbara, T.: Vertical Movements around Lake Biwa, Reprot of the Coordinating Committee for Earthquake Prediction, Vol. X, 1973, pp. 68-70.

2) Ohtake, M. and M. Katsumata: Detection of Premonitory Change in Seismic Wave Velocity, Proceedings of the National Symposium of the Earthquake Prediction Research in Japan, 1977, pp. 106-115.

3) Miki, H., A. Kuroiso, Y. Umeda, K. Ito K. Mino, F. Takeuchi, M. Imoto, K. Watanabe and N. Hirano: On the Activity of Earthquakes in the Area around Lake Biwa, Disas. Prev. Res. Inst. Annuals, Kyoto Univ., No. 19B-1, 1976, pp. 13-20.

4) Hashizume, M. Investigation of Microearthquakes— On the Nature of the Crust—, Bull. Disas. Prev. Res. Inst., Kyoto Univ., Vol. 20, Part 2, No' 172, Dec., 1970, pp. 53-64.

5) Mikumo T., M. Ôtsuka, T. Utsu, T. Terashima and A. Okada: Crustal Structure in Central Japan as Derived from the Miboro Explosion-Seismic Observations, Bull. Earthq. Res. Inst., Tokyo Univ., Vol. 39, 1961, pp. 327-349.

6) Wakayama Microearthquake Observatory: Seasonal Report of Wakayama Microearthq. Obs., Vol. 10, 1976.